

Development of microfluidic-based tools to mimic the human gastrointestinal tract

Patrícia Martins Rodrigues

UMinho | 2021



Universidade do Minho
Escola de Ciências

Patrícia Martins Rodrigues

Development of microfluidic-based tools to mimic the human gastrointestinal tract



julho 2021

Universidade do Minho
Escola de Ciências

Patrícia Martins Rodrigues

Development of microfluidic-based tools to mimic the human gastrointestinal tract

Master thesis

Master in Biophysics and Bionanosystems

Work developed under the supervision of

Dr Catarina Gonçalves

Prof. Dr Ana Arminda Lopes Preto Almeida

julho 2021

DIREITOS DE AUTOR E CONDIÇÕES DE UTILIZAÇÃO DO TRABALHO POR TERCEIROS

Este é um trabalho académico que pode ser utilizado por terceiros desde que respeitadas as regras e boas práticas internacionalmente aceites, no que concerne aos direitos de autor e direitos conexos.

Assim, o presente trabalho pode ser utilizado nos termos previstos na licença abaixo indicada.

Caso o utilizador necessite de permissão para poder fazer um uso do trabalho em condições não previstas no licenciamento indicado, deverá contactar o autor, através do RepositóriUM da Universidade do Minho.



Atribuição-NãoComercial-SemDerivações
CC BY-NC-ND

https://creativecommons.org/licenses/by-nc-nd/4.0/

Acknowledgements

Although it is my name that comes on the front cover of this thesis, the work here described would have never been possible if it was not for the help and understanding of my supervisors, my friends and my family. To all the people that somehow were involved in making this thesis possible, I am deeply grateful. Although many names will be left unsaid, I need to highlight some of the people that directly contributed to my welfare during this period of my life.

I would like to start by acknowledging Dr Catarina Gonçalves for the continued support and guidance throughout the entirety of this project. I'm really happy to have been part of this amazing team. To Ana Preto I am thankful for accepting to be my co-supervisor.

I am deeply grateful to Dr Miguel Xavier who took his time to guide me during these two years. I am extremely grateful for motivated me to be a better scientist, not to mention the patience he has when I was interrupting him to help me with minor things. It was my biggest pleasure to work with him, I learn so much. When I grow up, I want to be like him.

A special word of appreciation goes to my besties (Marisol, Micaela and Victor) for making my days at INL so much better. The greatest thank you to all of you for bringing me so much joy into my life and motivating me unconditionally every single day. To my friends and also lab buddies that I made during this journey (Ânia, Rita, Ana Martins, Arlete, Pedro, Gabriela, Inês, Yolanda, Alexandra, Célio and Maria Inês) I would like to thank for their support and availability to help me unconditionally.

The last words go to my parents and my siblings who were always with me in good and bad times and supported me in all decisions of my life. I also would like to thank my friends (Ana, Luísa, Carla e Adriana) for their continuous encouragement and never give up on me.

This work was carried out at the International Iberian Nanotechnology Laboratory (INL). It was supported by the MICRODIGEST project (grant agreement 037716) co-funded by FCT and ERDF through COMPETE2020

STATEMENT OF INTEGRITY

I hereby declare having conducted this academic work with integrity. I confirm that I have not used plagiarism or any form of undue use of information or falsification of results along the process leading to its elaboration.

I further declare that I have fully acknowledged the Code of Ethical Conduct of the University of Minho.

Desenvolvimento de ferramentas baseadas em microfluídica para replicar o trato gastrointestinal humano

Resumo

O desenvolvimento de novos nanomateriais capazes de transportar aditivos alimentares, ingredientes ou outros compostos bioativos, para administração oral, levanta questões relacionadas com a sua eficácia e segurança no corpo humano. Modelos *in vitro* robustos e confiáveis são de extrema importância para a realização de testes preliminares que precedam os modelos animais. A microfluídica permite o desenvolvimento de ferramentas capazes de efetuar estudos sobre a bioacessibilidade e permeabilidade intestinal de amostras, trazendo vantagens de operação e ao mesmo tempo reduzindo o consumo de amostra e reagentes e produção de resíduos. Este trabalho aborda o desenvolvimento de uma nova plataforma microfluídica modular, compreendendo um *digestion-chip* e um *gut-chip*. Os principais objetivos desta tese são: 1) estudar os fatores que influenciam a absorção de pequenas moléculas por dispositivos baseados em polidimetilsiloxano (PDMS), 2) estudar as modificações de superfície e matriz do PDMS com o objetivo de reduzir a absorção destas moléculas, 3) desenvolver um modelo de digestão *in vitro*, designado por *digestion-chip*, 4) obter culturas de células epiteliais intestinais robustas *on-chip*. Os estudos realizados demonstraram que diferentes fatores afetam a absorção de pequenas moléculas pelo PDMS, tais como a hidrofobicidade da molécula, o solvente e concentração do soluto usados e o tempo de residência determinado pela taxa de fluxo. Modificações de superfície e matriz foram testadas para prevenir a absorção. O seu sucesso e estabilidade foram avaliadas através da medição do ângulo de contacto de água. Quase todas as modificações testadas levaram a uma diminuição do ângulo de contato de água. No entanto, estas modificações foram transientes resultando numa reversão da hidrofobicidade natural do elastómero ao longo de 21 dias. Além disso, nenhuma das modificações testada resultou numa redução significativa da absorção das moléculas. Isto indicou que, quando a absorção de moléculas é problemática, materiais alternativos devem ser considerados para a fabricação de dispositivos. A digestão *on-chip* foi quantificada pela medição da intensidade de fluorescência de uma caseína *quenched* que se torna fluorescente após digestão. Embora a digestão tenha ocorrido numa menor extensão *on-chip*, quando comparado com o protocolo estático da INFOGEST, os resultados demonstraram ser consistentes e reprodutíveis e uma cinética de digestão resolvida no tempo foi obtida *on-chip*. No *gut-chip,* a morfologia das células Caco-2 foi avaliada por imunocitoquímica, marcando o núcleo, proteínas de junção (ocludina) e actina. Imagens confocais demonstraram uma monocamada de Caco-2 diferenciada com células epiteliais polarizadas com núcleos basais que melhor aproximam o epitélio intestinal humano.

No geral, este trabalho avalia o potencial de sistemas baseados em microfluídica como ferramentas *in vitro* para estudar a digestão e absorção de compostos funcionais desenvolvidos para administração oral, com o objetivo de diminuir a lacuna entre modelos dinâmicos complexos e os modelos estáticos simplistas.

Palavras-chave: Microfluídica, *lab-on-a-chip*, digestões *in vitro*, permeabilidade intestinal; *gut-chip*

Development of microfluidic-based tools to mimic the human gastrointestinal tract

Abstract

The development of new engineered nanomaterials to carry food additives, ingredients or other bioactive compounds, for oral administration, arise questions related with their efficacy and safety within the human body. Robust and reliable *in vitro* models are of utmost importance for a first screening before using animal models. Microfluidics offers the opportunity to create tools capable of outperforming studies concerning the bioaccessibility and intestinal permeability of samples with the advantage of having high throughput and a significant reduction of sample and reagent consumption and waste generation. This work addresses the development of a new modular microfluidic platform, comprising a digestion-chip and a gut-chip. The main goals of this thesis are: 1) to study the factors governing the absorption of small molecules by poly(dimethylsiloxane) (PDMS)-based devices, 2) to test surface and bulk modifications of PDMS aiming to reduce their absorption, 3) to develop an *in vitro* digestion model, called digestion-chip, and 4) to achieve robust epithelial intestinal cell cultures on-chip. The studies performed demonstrated that different factors affect the absorption of small molecules by PDMS, such as the hydrophobicity of the molecule, the solvent and solute concentrations used, and the residence time determined by the flow rate. Surface and bulk PDMS modifications were tested to avoid absorption. Their success and stability were evaluated through the measurement of the water contact angle over time. Almost all tested modifications led to a decreased water contact angle. However, these modifications showed a transient effect with the elastomer reverting to its original hydrophobic nature over the course of 21 days. Furthermore, none of the modifications were able to achieve a significant reduction of the absorption of tested molecules. This indicated that when molecule absorption is deemed to be problematic, alternative materials may be considered for device fabrication. On-chip digestion was quantified by measuring the fluorescence of a quenched-casein that becomes fluorescent after digestion. Although digestion occurred to a lower extension on-chip when compared to static INFOGEST protocol, the results showed consistency and reproducibility and a time-resolved digestion kinetics was obtained on-chip. In the gut-chip, the morphology of Caco-2 cells was assessed by immunocytochemistry, staining nuclei, tight-junctions (occludin) and actin. Confocal images showed a differentiated Caco-2 monolayer revealing polarised epithelial cells with basal nucleus that better approximates the human intestinal epithelium.

Overall, this work evaluates the capacity of microfluidics-based systems as *in vitro* tools to study the digestion and absorption of functional compounds designed for oral administration, aiming to bridge the gap between the convoluted dynamic models and simplistic static models.

Keywords: Microfluidics, lab-on-a-chip, *In vitro* digestion, intestinal permeability, gut-chip

Contents

List of Figures ..... **ix**

List of Supplementary Figures ..... **xiii**

List of Tables ..... **xiv**

List of Supplementary Tables ..... **xv**

List of Abbreviations ..... **xvi**

1. Introduction **1**

1.1 Background 1

1.2 Microfluidic Technology 5

1.2.1 Physics of Microfluidics 5

1.2.2 Microfluidic Devices 6

1.2.3 Description of Microfabrication Techniques 9

1.2.3.1 Photolithography 9

1.2.3.2 Soft lithography and Bonding 10

1.3 Microfluidic-based *in vitro* models 11

1.3.1 Digestion 11

1.3.2 Intestinal Permeability 11

2. Project Goals and Strategy **16**

3.Materials and Methods **17**

3.1 Materials 17

3.2 Device Design 18

3.3 Device Fabrication 19

3.3.1 Digestion-chip 19

3.3.2 Gut-chip 20

3.3.2.1 PDMS Membrane 20

3.4 PDMS Modification 21

3.4.1 Surface Modification 21

3.4.1.1 Pluronic F-127 21

3.4.1.2 (3-Aminopropyl)triethoxysilane (APTES) 21

3.4.2 Bulk Modification of PDMS 21

3.4.2.1 Gradient-Induced Migration of Embedded Pluronic 21

3.4.2.2 Thermal Aging 22

3.4.2.3 Extraction of Uncrosslinked Contaminants using Organic Solvents 22

3.4.2.4 Sol-Gel Treatment 22
3.5 Absorption Study 22
3.6 Contact Angle Measurements 23
3.7 *In Vitro* Digestion 23
3.7.1 Static Digestion 24
3.7.2 On-chip Digestion 25
3.7.3 Mixing by Chaotic Advection 25
3.8 Gut Chip Culture 25
3.8.1 Cell Culture 25
3.8.2 Cell Seeding On-chip 25
3.8.3 Immunocytochemistry 26
3.9 Statistical Analysis 26
4. Results and Discussion 27
4.1 Absorption studies 27
4.1.1 Molecule partitioning as a function of solute/solvent pairings 27
4.1.2 Molecule partitioning as a function of residence time 29
4.1.3 Molecule partitioning as a function of concentration 30
4.2 PDMS modification aiming to reduce molecules absorption 32
4.2.1 Water contact angle studies 32
4.2.2 Absorption studies 33
4.3 On-chip *in vitro* digestion 35
4.3.1 Mixing by chaotic advection 36
4.3.2 Enzyme kinetics 37
4.3.3 On-chip digestion vs static *in vitro* protocol 38
4.3.4 Time-resolved digestion on-chip 39
4.4 Cell Seeding on-chip 40
5. Conclusions and Future Perspectives 45
6. References 46
7. Annexes 55

List of Figures

Figure 1. (A) Schematic representation of the standardised INFOGEST protocol for static in vitro digestion. (B) The TNO dynamic in vitro model of the colon – TIM-2. Image used with permission from Nicola Twilley, Gastropod Podcast. Listen to the accompanying episode here: https://gastropod.com/guts-and-glory/.[13] 2

Figure 2. (A) Simplified model of the intestinal epithelium evidencing the typical villi structures, abundant enterocytes and mucous-producing goblet cells. (B) Transport across the intestinal epithelium: 1 – passive transcellular transport; 2 – passive paracellular transport; 3 – active carrier-mediated transport; 4 – transcytosis; 5 – efflux transporters.[13] 3

Figure 3. Optical microscopy images of Caco-2 cells at passage 28 grown in tissue culture flasks. (A) 4x and (B) 10x magnification. 4

Figure 4. Microfluidic Gut-chip platforms. (A-B) The NutriChip developed at EPFL used multiple chambers to the activation of immune cells in response to the transfer and processing of nutrients across the epithelial cell layer. Image was adapted with permission from Ramadan et al.[102] C) HuMiX uses 3 parallel chambers separated by 2 microporous membranes to allow the co-culture of the intestinal epithelium with anaerobic bacteria [103]. D) The Gut-Chip from the Wyss Institute simulates peristalsis-like movements by the application of vacuum to two hollow chambers that line the whole length of the fluidic channels. Images adapted with permission from Kim et al.[88] and Firoozinezhad et al.[116] 15

Figure 5. (A) Schematic representation of the digestion-chip design, (B) staggering herringbone micromixers (SHMs) to allow the mixing between the sample and the simulant salivary fluid, (C) SHMs to allow mixing of chyme and simulant intestinal fluid, (D) visualisation of the mixing seen by the colour change as the different dyes are being introduced in the SHMs (E) 3D representation of the digestion-chip and (F) gut-chip design (top and bottom slab). 18

Figure 6. Fabrication of the digestion-chip. Silicon master mould of the (A) stomach and intestinal incubation compartments and (B) staggering herringbone micromixers. 19

Figure 7. SEM images of silicon master moulds with micropillar arrays. Images were taken by the International Iberian Laboratory Nanotechnology (INL), Portugal, cleanroom staff. 21

Figure 8. Schematic representation of the device operation. Created with Biorender. 23

Figure 9. Confocal microscopy images of (A) 1 μM Nile Red, (B) 1 μM Rhodamine B and (C) 1 μM Fluorescein absorption into a PDMS channel wall at 96 $\mu L \cdot h^{-1}$. Each image represents one slice of a z-stack taken over a 1.5 mm-high section of the PDMS channel and acquired at 50 μm increments. 28

Figure 10. Percentage (%) of 1 μM Nile red in ethanol and Rhodamine B and Fluorescein in PBS remained in solution after 90 min flowing through the PDMS microfluidic channel at 96 μL·h^{-1}. Values show mean and standard deviation of three independent experiments. 28
Figure 11. Nile Red absorption by PDMS as a function of the solvent used. Percentage (%) of Nile red remained in solution after flowing 1 μM Nile red in ethanol or 0.3 μM in ethanol/PBS through the microfluidic device for 90 min at 96 μL·h^{-1}. Values show the mean and standard deviation of three independent experiments; ***$p < 0.001$ with p-values obtained using the Student's t-test that followed a normal distribution according to the Shapiro-Wilk test. 29
Figure 12. Nile Red absorption by PDMS as a function of the residence time. Percentage (%) of Nile Red remained in solution after the first passage of Nile red in ethanol/PBS (1:3 ratio) through the microfluidic channel at a flow rate of 400 μL·h^{-1} and 1000 μL·h^{-1}. Values show the measurement of one independent experiment. 30
Figure 13. Confocal images showing the absorption of Rhodamine B into the PDMS channel wall after the flow of (A) 1 μM and (B) 20 μM solutions. 31
Figure 14. Rhodamine B absorption by PDMS as a function of concentration. Percentage (%) of rhodamine B remained in solution after flowing 1 μM or 20 μM Rhodamine B at 400 μL·h^{-1} collecting a sample every 30 min. Values show the measurement of one independent experiment. 31
Figure 15. Relation of the water contact measurements as a function of time of (A) surface and (B) bulk modified PDMS. Values show mean and standard deviations from at least 3 independent measurements. 32
Figure 16. Percentage (%) of Nile Red remained in solution after flowing 1 μM Nile Red in ethanol/PBS (1:3 ratio) on unmodified PDMS, (A) PDMS surface modified with 3% Pluronic F-127, (B) PDMS bulk modified with Pluronic F-127, (C) PDMS modified with 14 days of thermal aging and (D) PDMS modified with organic solvents. Values show mean and standard deviation from a minimum of two independent experiments; ***$p < 0.01$, p-values obtained using a two-way analysis of variance (ANOVA) with Tukey's post-hoc test. 33
Figure 17. Fluorescence intensity profiles obtained from the confocal micrographs after flowing 20 μM Rhodamine B on (A) unmodified PDMS and (B) bulk modified PDMS with sol-gel treatment. These line profiles were acquired after 240 min of flow at 400 μL·h^{-1}. 34
Figure 18. Percentage (%) of digested casein remained in solution after flowing through the digestion-chip for 300 min at 96 μL·h^{-1}. Values show the mean and standard deviation of three samples of one independent experiment. 35

Figure 19. Performance of the mixing process in micromixers with herringbone-shaped grooves. (A) Confocal micrograph of fluorescein (5 μM in water) being continuously mixed with water (0 μM) as the mixing proceeds along the microchannel. (B-C) Top and orthogonal cross-section views of the fluorescence intensity distribution upstream of the features, respectively. (D) Fluorescence intensity profiles extrapolated from cross sections after one cycle, two half cycle, four cycles, six cycles and seven half cycles.. 36

Figure 20. Enzymatic kinetics studies were performed throughout the microfluidic channel to demonstrate the catalysis function. The solution containing the varying concentration of substrate, [S], was introduced in one micromixer inlet, and the simulant gastric fluid containing a fixed concentration of enzyme, [E], was introduced in the other inlet. Fluorescence signals of casein-catalysis digestion of (A) 2 $\mu g \cdot mL^{-1}$, (B) 5 $\mu g \cdot mL^{-1}$, (C) 10 $\mu g \cdot mL^{-1}$, (D) 20 $\mu g \cdot mL^{-1}$ and (E) 50 $\mu g \cdot mL^{-1}$ of substrate in the stomach compartment and (F) fluorescence intensity as a function of substrate concentration in the end of the digestion-chip. Values show the measurement of one independent experiment. 37

Figure 21. Extension of digestion following the static INFOGEST protocol of casein reporter molecule at 1 and 10 $\mu g \cdot mL^{-1}$ and its comparison with the end-point of a full digestion of using our digestion-chip (green triangles).. 39

Figure 22. Time-resolved digestion obtained on-chip by varying the flow rates (12-1152 $\mu L \cdot h^{-1}$) of the sample and simulated digestion fluids thus attaining different incubation times. 40

Figure 23. Tile scan confocal micrographs 40x magnification of Caco-2 cells growth on 1 μm pore size transwell® inserts, stained for nuclei (DAPI, blue), tight junctions (occludin, green) and actin filaments (phalloidin, red). Images were acquired after 7, 14 or 21 days in culture. 42

Figure 24. Metabolic activity of Caco-2 cells grown on tissue culture polystyrene (TCPS), unmodified PDMS (PDMS), PDMS treated with oxygen plasma (PDMS + O_2) and PDMS treated with oxygen plasma and coated with ECM (30 $\mu g \cdot mL^{-1}$ collagen type-I and 100 $\mu g \cdot mL^{-1}$ Matrigel) (PDMS + O_2 + Collagen + Matrigel) after 48 h. The cell metabolic activity was determined by the resazurin reduction assay measuring the fluorescence of resorufin (λ_{ex}= 560 nm, λ_{em}= 590 nm). Values show mean and standard deviation of three independent experiments; $^{**}p < 0.01$;$^{***}p < 0.001$ with p-values obtained using the Student's t-test that followed a normal distribution according to the Shapiro-Wilk test. 42

Figure 25. Confocal image of ECM coating on PDMS membrane stained against laminin (the main component of matrigel) in the gut-chip. 43

Figure 26. Confocal micrographs 10x magnification of Caco-2 cells grown on the gut-chip and stained for nuclei (DAPI, blue), tight junctions (occludin, green) and actin filaments (phalloidin, red). Images were acquired after 4 or 7 days with continuous flow (30 μL·h^{-1}.) in the gut-chip..... 43
Figure 27. Confocal images and orthogonal cross-section views of Caco-2 cells grown on (A) Transwell inserts after 21 days in culture and (B) gut-chip after 7 days of continuous flow (30 μL.h^{-1}), stained for occludin (green), nuclei (DAPI, blue) and f-actin (red). Bar in the orthogonal images corresponds to 30 μm..... 44

List of Supplementary Figures

Figure S1. Graphic representation of fluorescence spectra of (A) Nile Red solution in ethanol; (B) Nile Red solution in ethanol/PBS; (C) Fluorescein solution; (D) Rhodamine B solution.The excitation and emission maxima of Nile Red in ethanol (λ_{ex}: 543 nm; λ_{em}: 627 nm), Nile Red in ethanol/PBS (λ_{ex}: 584 nm; λ_{em}: 650 nm); Fluorescein (λ_{ex}: 485 nm; λ_{em}: 515 nm) and Rhodamine B (λ_{ex}: 550 nm; λ_{em}: 580 nm). 55

Figure S2. Enzymatic kinetics studies were performed throughout the microfluidic channel to demonstrate the catalysis function. The solution containing the varying concentration of substrate, [S], was introduced in one micromixer inlet, and the gastric simulant fluid containing a fixed concentration of enzyme, [E], was introduced in the other inlet. Fluorescence signals of casein-catalysis digestion of 100 $\mu g m L^{-1}$ of substrate in the stomach compartment. Values shows the measurements of one independent experiment.....56

Figure S3. Confocal micrographs showing casein aggregates in the gastric and intestinal chamber after the flow of casein digested off-chip for 300 min.....57

Figure S4. Fluorescence image of Caco-2 cells adherence on (A) tissue culture polystyrene (TCPS), (B) PDMS treated with oxygen plasma (PDMS + O_2) and (C) PDMS treated with oxygen plasma and coated with ECM (30 $\mu g \cdot mL^{-1}$ collagen type-I and 100 $\mu g \cdot mL^{-1}$ Matrigel) (PDMS + O_2 + Collagen + Matrigel) after 48 h of culture.....57

List of Tables

Table 1. Microfabrication specifications for the fabrication of the silicon master moulds used for PDMS casting of the digestion-chip devices. Features with 20 and 80 μm were used to fabricate the staggering herringbone micromixers, 250 μm to fabricate the stomach compartment and 500 μm to fabricate the small intestine compartment..... 20

Table 2. Volumes of electrolyte stock solutions of simulated digestion fluids for a volume of 400 mL diluted with water (1.25× concentrated). Owing to the gas permeability of PDMS, both static and digestion-chip were performed considering as open systems. Following the recommendations of Brodkorb et al.[116], sodium bicarbonate ($NaHCO_3$) was replaced with NaCl at the same molar ratio to ensure the ionic strength of the electrolyte solutions (oral, gastric and intestinal) which was proven to be effective in avoiding undesirable pH drift. Important to note that the $CaCl_2(H_2O)_2$, pepsin, pancreatin and bile salts were added immediately before the experiment. 24

Table 3. Evaporation (%) of ethanol (density 0.789 g/mL) while flowing through the microfluidic channel for 150 min at 96 $\mu L \cdot h^{-1}$.....28

List of Supplementary Tables

Table S1. Calculations of the Reynolds number ($Re=\rho \cdot V \cdot D/\mu$) at a range flow rates used in the GIT-on-a-chip digestion considering the channel dimensions at the staggered herringbone regions (200 μm x 100 μm), the hydraulic diameter (D) estimated at $2h \cdot w/h+w$. The density ($\rho=0.9982x10^{3}$ $kg \cdot m^{-3}$) and dynamic viscosity ($\mu=1.002x10^{-3}$ $Pa \cdot s$) of water at 20 °C were used. 55

List of Abbreviations

μPADs	Microfluidic paper-based analytical devices
μ-TAS	Miniaturised total analysis systems
APTES	3-aminopropyl)triethoxysilane
BSA	Bovine serum albumin
DAPI	4′, 6-diamidino-2-phenylindole, dilactate
diH_2O	Deionised water
DMEM	Dulbecco's modified Eagle's Medium
DMSO	Dimethyl sulfoxide
ECM	Extracellular matrix
EDTA	Ethylenediamine tetraacetic acid
FBS	Foetal bovine serum
GI-μCCA	Gastrointestinal tract micro cell culture analogue
GIT	Gastrointestinal tract
hIECs	Human intestinal epithelial cells
HuMiX®	Human-Microbial Crosstalk
LOC	Lab-on-a-chip
Log P	Coefficient partition
MEM	Minimum essential media
MEMS	Microelectromechanical systems
O_2-plasma	Oxygen plasma
PBS	Phosphate-buffered saline
PBMCs	Peripheral blood mononuclear cells
PDMS	Poly(dimethylsiloxane)
PEO-PPO-PEO	Poly(ethylene oxide), poly(propylene oxide), and poly(ethylene oxide
P-F127	Pluronic F127
PFA	Paraformaldehyde
Phalloidin-TRITC	Phalloidin-tetramethyl rhodamine B isothiocyanate

PMMA	Poly(methylmethacrylate)
PS	Polystyrene
SEM	Scanning electron microscopy
SGF	Simulated gastric fluid
SHIME®	Simulator of the Human Intestinal Microbial Ecosystem
SIF	Simulated intestinal fluid
SSF	Simulated salivary fluid
Sulfo-SANPAH	Sulfosuccinimidyl 6-(4'-azido-2'-nitrophenylamino
TEER	Trans-epithelial electrical resistance
TEOS	Tetraethyl orthosilicate
TIM®	TNO (gastro-) Intestinal Model

1. Introduction

1.1 Background

Food-derived bioactive compounds have been associated with functional properties including antioxidant, anti-inflammatory, anticarcinogenic and antimicrobial effects[1,23,4]. However, the application of bioactive compounds in food science by oral delivery is restricted by their low digestion stability (bioaccessibility), low gastrointestinal absorption (bioavailability) and instability during processing and storage[4,5]. To overcome these challenges, the development of nanostructures has gained interest in the encapsulation of nutrients and bioactive compounds aiming to improve their stability as well as bioaccessibility and bioavailability during passage through the gastrointestinal tract[6–8].

During human digestion, nutrients or bioactive compounds must be released from the food matrix in order to be absorbed through the intestinal epithelium to the systemic circulation[1,2]. Therefore, a successful development of new formulations is strongly associated with the capacity of compounds to cross the epithelial barrier and enter the bloodstream without causing any toxicity.

Understanding the digestibility and the release of bioactive compounds from food matrices or delivery systems and thus their bioaccessibility (fraction available to be absorbed in the small intestine) have been accomplished through *in vitro* digestion methods[1].

In vitro digestion models have emerged as an alternative to human and animal studies to reduce associated costs, intricate approaches and ethical concerns[2]. Generally, *in vitro* digestion models can be divided into static and dynamic models.

Static models are the most predominant owing to their simplicity and easy access. The traditional static model comprises containers in a water/air bath at 37°C, pH changes according to the digestion phase, and consistent shaking to mix samples with digestive enzymes and simulant fluids[9]. The absence of a consensus in adequate physiological conditions has contributed to incomparable results between research teams[2]. Currently, the standardised protocol developed by the INFOGEST COST action is considered the gold standard for static simulation of digestion, which comprises a sequential oral, gastric and intestinal phases, where pH, digestion time, type and activity of enzymes, bile concentration, sample dilution, and simulant fluids were defined based on available physiological data[1010] (Figure 1A). Although, static models are simple and provide valuable information to preliminary trials, the digestion process includes contributions from the dynamic environment of the gastrointestinal tract that lead to noticeable limitations of these models[2].

Dynamic models offer the opportunity to perform a more complex digestion that replicates more closely the *in vivo* scenario. These models implement continuous flow and automatic pH adjustments, peristaltic movements, enzyme addition, and microbiological fermentation[9]. Some computerized sophisticated models, such as TNO gastrointestinal model (TIM)[11] and SHIME[12] were developed in the early 90's combining the physiological processes within the stomach and the small intestine. These multi-compartmental systems evolved over time providing valuable information about the digestibility of complex food matrices[13]. Recently, a dynamic Gastrointestinal Simulator was developed at the Institute of Food Science Research (CIAL, Spain)[14] and incorporates the possibility of replicating the colonic fermentation processes responsible for metabolic bioconversion[15,16]. However, these models are highly complex, time-consuming, require high amounts of expensive enzymes and reagents, and lack the finesse to study the bioaccessibility of valuable molecules in small volumes. Furthermore, the complexity of food matrices also hinders the detection of nanoformulations. The selection between models typically requires a compromise between technological complexity and biological significance[13].

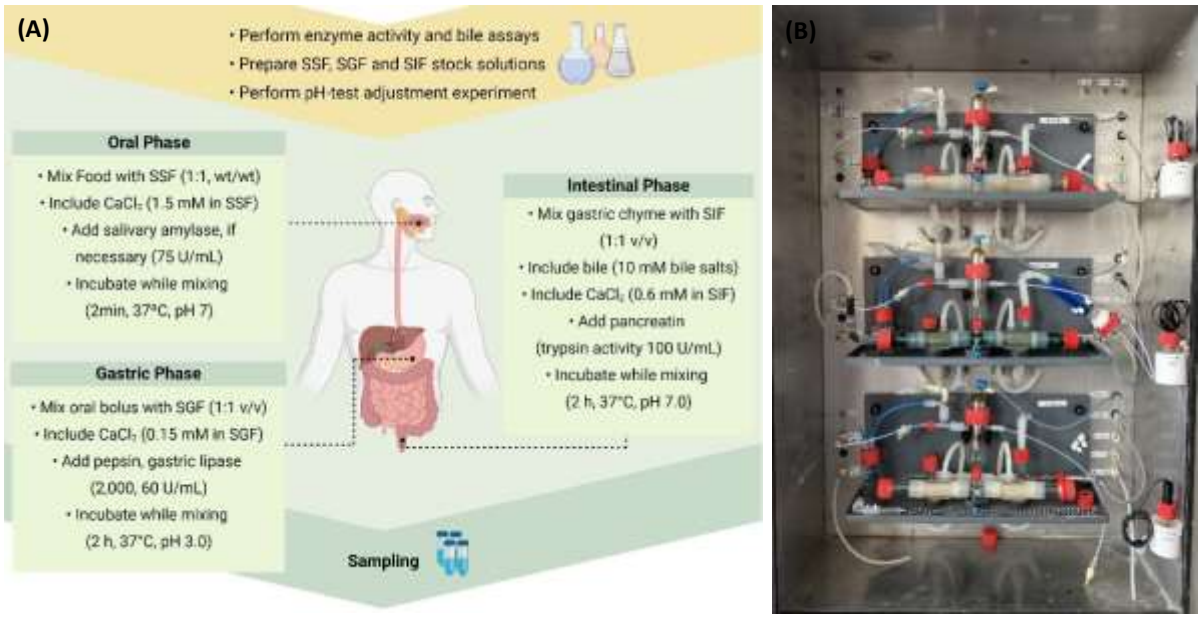

Figure 1. (A) Schematic representation of the standardised INFOGEST protocol for static in vitro digestion. (B) The TNO dynamic in vitro model of the colon – TIM-2. Image used with permission from Nicola Twilley, Gastropod Podcast. Listen to the accompanying episode here: https://gastropod. com/guts-and-glory/.[13]

As an important step towards determining the bioaccessibility of a bioactive compound, it is important to evaluate their intestinal permeability through the intestinal epithelium. Reliable intestinal permeability models should integrate a polarised epithelium with relevant phenotypes and a variety of metabolic pathways and transport mechanisms that regulate transport across the intestinal barrier. These mechanisms can be classified as passive or active (energy-dependent) transport, and by relying on the transcellular or paracellular route corresponding to transfer across cells and between adjacent cells, respectively (Figure 2)[17].

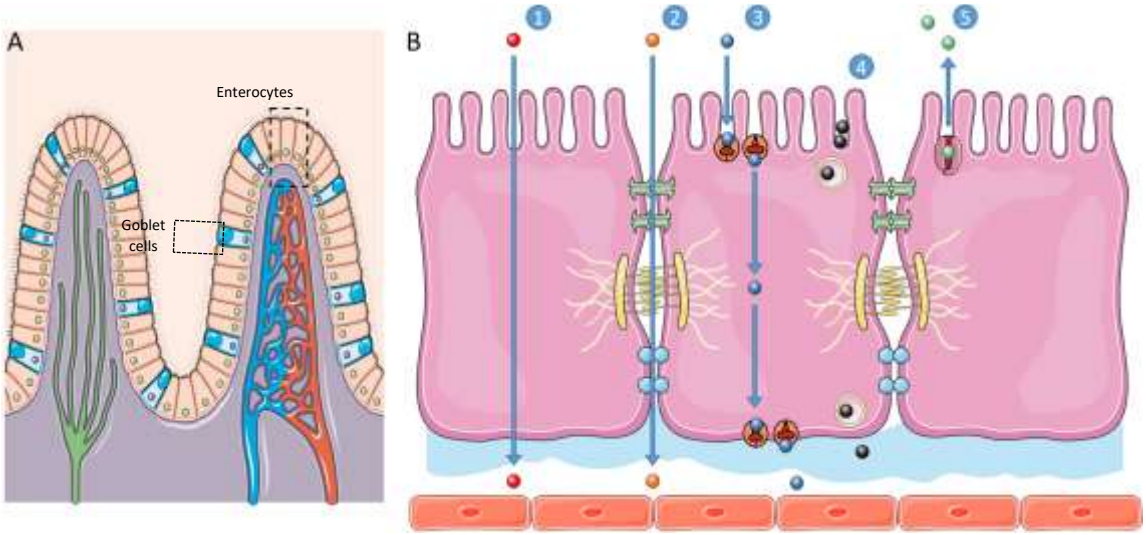

Figure 2. (A) Simplified model of the intestinal epithelium evidencing the typical villi structures, abundant enterocytes and mucous-producing goblet cells. (B) Transport across the intestinal epithelium: 1 – passive transcellular transport; 2 – passive paracellular transport; 3 – active carrier-mediated transport; 4 – transcytosis; 5 – efflux transporters.[13]

Enterocytes are the most abundant cell type in the human intestinal epithelium and are responsible for the absorption of nutrients. Caco-2 cells, from human colorectal carcinoma, (Figure 3) are considered the gold standard to mimic the intestinal epithelium and thus study the intestinal permeability of tested substances through the human gut[18–20]. Upon reaching confluency, Caco-2 cells spontaneously differentiate into a polarised epithelium with microvilli tightly sealed by tight junctions and expressing typical metabolic enzymes and membrane uptake/efflux transporters[21,22]. Monitoring the trans-epithelial electrical resistance (TEER) across the monolayer provides information about the barrier integrity, which reflects permeability across the paracellular route. This can also be achieved, perhaps more reliably, by measuring permeability directly using paracellular markers, such as Lucifer yellow[23]. However, Caco-2 show lower paracellular permeability values than those observed *in vivo*[20,22,24]. Another disadvantage of Caco-2 relates to the lack of mucus production, which means that small molecules have easier access to microvilli.

To better approximate the physiology of the intestinal mucosa, co-cultures of Caco-2 cells with other cell types have become common practise in research. A relevant example is the co-culture with HT29-MTX[25], representing mature goblet cells - the second most abundant cell type in the human intestinal epithelium - to form a mucus layer[26–30]. Co-cultures of Caco-2/HT29-MTX, usually in a 1:9 ratio, improve Caco-2 paracellular permeability and promote a decrease in the TEER and P-glycoprotein expression, leading to a better correlation to what is observed in humans or animals *in vivo*[26].

Complex models have evolved using triple co-cultures. For example, Raji B lymphocytes are usually cultured in combination with Caco-2 and HT29-MTX cells to promote the differentiation of Caco-2 cells into M cells[31]. M cells, which comprise less than 1% of the surface area of the intestinal epithelium, are present in Peyer's patches and are specialised in antigen uptake and sampling contributing to the mucosal immune response[26,31]. Human myofibroblasts (CCD-18Co) embedded in Matrigel are another example of cells used in triple co-culture models[32]. CCD18-Co myofibroblasts mimic the intestinal *lamina propria* underlying epithelial cells as they produce their own ECM matrix. The authors demonstrated a more reliable prediction of insulin absorption by the intestinal epithelium when compared to Caco-2/HT29-MTX co-cultures.

Finally, the gut microbiome plays an important role in nutrient digestion, drug metabolism, and immune system, contributing to gut homeostasis. In fact, recent research indicates that the number of bacteria in the human body is higher than that of human cells, with most of them residing in the gut. However, long-term co-cultures with commensal gut microbiome under static culture conditions is limited because the microbiota overgrows eukaryotic cells compromising their viability. Another aspect that transversely limits the *in vivo* correlation of 2D *in vitro* intestinal models is the inability to replicate the complex process of digestion that precedes absorption at the intestinal epithelium[22].

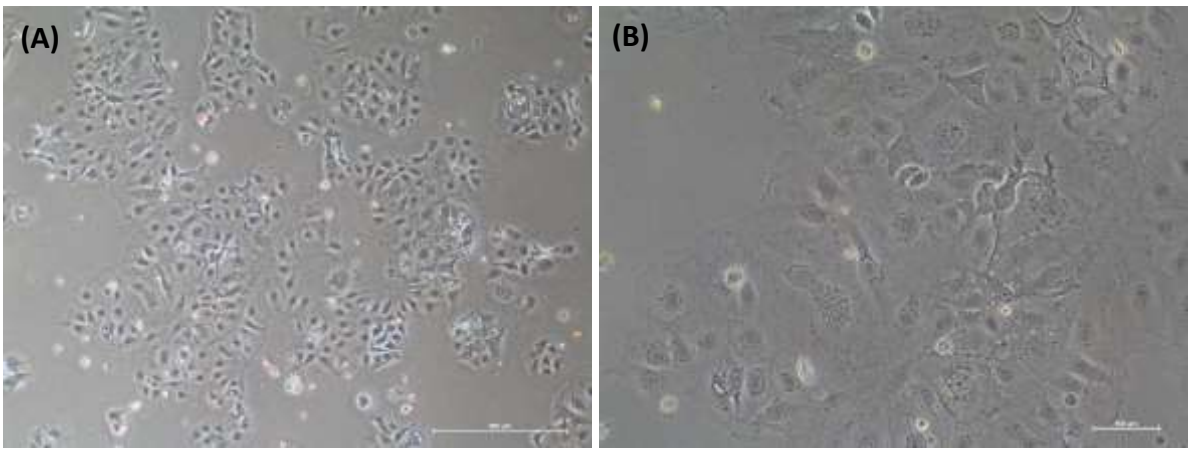

Figure 3. Optical microscopy images of Caco-2 cells at passage 28 grown in tissue culture flasks. (A) 4x and (B) 10x magnification.

While the *in vitro* models described to date have added to the understanding of the bioaccessibility and intestinal permeability of several interesting compounds, they have been limited by overlooking important aspects of the gut physiology, including peristalsis or continuous flow. The development of microfluidic devices based on organ-on-a-chip technology has allowed great advances in science research, since these devices represent a potential approach to replicate complex structures and functions of human organs, therefore establishing more realistic physiological models.

1.2 Microfluidic Technology

Microfluidics emerged from the development of microelectromechanical systems (MEMS) that were originally designed to be used in the areas of physics and engineering[33]. The evolution of this technology in the creation of microfluidic platforms referred to as miniaturised total analysis systems (μ-TAS) or Lab-on-a-chip (LOC), allowed the manipulation of extremely small fluid volumes (10^{-9} to 10^{-18} liters) in microchannels spanning micrometre dimensions[33–37]. The significant growth of microfluidics permitted its use in several biological fields comprising biochemistry, cell signalling, drug testing, genomics, and proteomics[38]. Several advantages of microfluidics are based on fast analysis, high throughput, low reagent consumption, reduced waste product, high sensitivity, and great portability when compared to other technologies[33].

1.2.1 Physics of Microfluidics

In miniaturised systems, the physical principles comprising mechanics, fluid dynamics, and thermodynamics are well known. However, dealing with reduced channel dimensions changes the interplay among forces and their relative importance[39]. The dimensionless Reynolds number (Re) allows to define whether flow is in the laminar or turbulent regime[40] by comparing the magnitude of inertial and viscous forces. Re can be expressed as follows[41]:

$$Re = \frac{\rho v L}{\mu} \quad (equation\ 1)$$

Where ρ is the density of the fluid, v the average flow velocity, L the characteristic length scale of the system, and μ the fluid dynamic viscosity. A Reynolds number below 2,000 typically indicates a laminar flow, while the fluid dynamics enter an intermediate regime between 2,000 and 3,000 and change to a turbulent flow above 3,000[39].

In microfluidics, the behaviour of fluids is closely related to the scaling effect[42]. At the microscale, flow is almost always laminar, and typical Re ranges from 10^{3} to 10^{0} predicting that viscosity dominates over inertia[39]. The laminar regime leads to a highly predictable flow in which particles in two or more fluid streams remain parallel to each other. Without a physical separation, particles may still diffuse freely from one stream to the other[41]. This physical mechanism can be described by the tendency of a concentrated group of particles to move to regions of lower concentration due to Brownian motion. Considering diffusion as the only dimension, the equation can be expressed as[39]:

$$d^2 = 2Dt \quad (equation\,2)$$

Where d corresponds to the distance travelled by a particle in a specific time t, and D to the molecular diffusion coefficient of the material. However, diffusion can often be neglected since the diffusion time is normally larger than the time needed for a particle to cross the entire microfluidic channel[39]. The Peclet number relates advective transport with diffusion and is described as follows[41]:

$$Pe = \frac{vL}{D} \quad (equation\,3)$$

Here, v is the average flow velocity and L the typical length scale of the microchannel[39]. As with the Reynolds number, the small dimensions of microchannels imply low Peclet[42]. In addition, surface effects interfere with flow at the microscale with surface tension and capillary forces gaining prominence, eventually even dominating over gravity and allowing the movement of fluids without pumps[39].

1.2.2 Microfluidic Devices

Microfluidic devices were initially developed using inorganic materials, such as silicon and glass. Silicon was the first substrate used to fabricate microfluidic devices using photolithography, additive methods (e.g., thin-film deposition), subtractive methods (e.g., etching) and substrate bonding[43]. Silicon has a well-developed surface chemistry offering excellent surface stability, solvent compatibility, and good chemical resistance, favouring its use in many applications[42,44]. Surface modification can be accomplished using silanes to reduce nonspecific adsorption or improve cellular growth[45]. However, silicon is not transparent to visible light limiting its use in optical detection applications, and its high elastic modulus becomes inconvenient for the manufacture of active fluidic components, such as valves and pumps[45]. To add to these drawbacks, silicon-based fabrication of microfluidic devices involves expensive processes, is limited to flat surfaces, and requires specialized installations[35].

Owing to its transparency, glass enabled the incorporation of light-based detection methods leading to a new generation of optical microfluidic biosensors[42]. Glass is also more compatible with electro-osmotic flow arguably attributed to its lower electroconductivity[46]. Photolithography[47] and etching (e.g., reactive ion etching and wet etching) are common methods for the fabrication of glass-based microfluidic devices, thus being equally high cost and time-consuming[48].

Opposite to these inorganic materials, paper and polymers have been used as alternative substrates to overcome some limitations associated with these materials. Paper, a cellulose-based material[45], has emerged as a promising substrate for microfluidics applications given its advantages, such as straightforwardness and economic affordability. Microfluidic paper-based analytical devices (μPADs) can be used in diagnostic biosensing, food safety applications and environmental monitoring[49,50]. Paper is also thin, lightweight, biocompatible, suitable for colorimetric tests and can be chemically modified[51]. For the fabrication of μPADs, hydrophilic channels with hydrophobic barriers can be patterned on paper using several methods including photolithography, plotting, inkjet etching, plasma etching, cutting and wax printing[52]. However, some diagnostic and monitoring applications are limited in these devices since paper has low mechanical resistance and surface tension[49].

Microfluidic devices based on different polymers have attracted increasing attention in the microfluidic community due to their low-cost, ease of processing, and intrinsic properties, such as mechanical strength, optical transparency and chemical stability[53]. Polymer materials include thermoplastics, such as polystyrene (PS) and poly(methylmethacrylate) (PMMA) and elastomers like poly(dimethylsiloxane) (PDMS)[54]. Thermoplastics are normally durable, resistant to absorption of small molecules, stiffer than elastomers,[45] and suitable to be mass-produced via either hot embossing or injection moulding[55].

Towards the late 1990s[45], George Whitesides and his group at Harvard introduced PDMS as a promising material for the fabrication of microfluidic devices[42]. Since then, PDMS became the most common substrate used in several research fields.[56] It is widely described because of its low cost, rapid prototyping and ease of patterning using soft lithography techniques, representing a nonphotolithographic strategy based on replica moulding[43]. The PDMS structure consists of an inorganic siloxane backbone and organic methyl groups attached to silicon ($O\text{-}Si(CH_3)_2$)[40] which leads to a unique combination of interesting properties:

-**Optical transparency.** PDMS is optically transparent within the 240-1100 nm range,[57] which makes it suitable for optical applications[40]. Despite the high transmittance PDMS is still slightly fluorescent though less than other polymer materials, and thus still allowing health and motility monitorisation of cells using together bright field and fluorescence microscopy, for example[58].

-**Biocompatibility.** PDMS does not produce unwanted consequences on biological samples[59,60] being a suitable reference for cell culture, organ-on-chip, and biomedical implants[40,61]. PDMS may also resolve the compatibility of microfluidic devices made from other materials when used as a coating[40].

-**Gas permeability**. Permeability to gases offers a relevant advantage since it allows the diffusion of CO_2 and O_2 from cells through the PDMS matrix. Based on reported diffusion coefficients, the oxygen permeability of PDMS is three orders of magnitude higher than other polymers. The high permeability of PDMS to water vapour can also introduce some drawbacks in microfluidic applications attributed to evaporation[40,62]. At the microscale, evaporation becomes more prominent because of the small volumes used, with small amounts of evaporation significantly affecting volumes, concentrations, chemical balances, critical gradients and other factors[63].

-**Inert material.** Chemically inert surfaces become particularly interesting by enabling the spatial patterning of proteins or cells. Microcontact printing, creates patterned substrates through the contact of a PDMS stamp with a solution containing the patterning components (e.g., molecules, polymers or proteins), and later transferring the 'ink' to another PDMS layer or a different substrate, such as glass[40,64]. Using microcontact printing, microfluidic devices have been used for tissue engineering or biosensing applications where cells are restricted into a specific region of a substrate with well-defined control of their size and shape[40].

-**Deformation.** An advantage frequently associated with PDMS refers to its high compliance, or low stiffness[63]. PDMS has an elastic modulus of ~1-3MPa, which is four orders of magnitude lower than glass (~50GPa) and three orders of magnitude lower than PS (~3 GPa)[65]. PDMS deformation facilitates demoulding during fabrication[66] and allows a reliable bonding with other surfaces. Owing to its high compliance, several applications have been developed to actively apply cell stretching in microsystems[67], and to measure cell traction forces[68] or biological responses to substrate deformation[69]. Besides, the creation of integrated valves and pumping systems introduced high-density multiplexing[70] and fluidic control[71] providing a significant development for the miniaturisation and large-scale integration of automated systems[72]. However, the high compliance of PDMS can also introduce some disadvantages when channels deform and bulge under pressure-driven flow and thus affecting the actual flow rate due to modifications in cross-sectional area[73] .

-**Absorption**. The hydrophobicity of PDMS prone to the absorption of nonpolar organic solvents[74] and small hydrophobic molecules into the polymer matrix[75]. These issues contribute to changes in the local concentration of solutes inside the microfluidic channels and consequently may inadvertently and negatively influence experimental conditions[76]. Reducing the absorption of small hydrophobic compounds and preserving the molecules inside the channels may be achievable through coatings or chemical modifications of the microfluidic channels.

1.2.3 Description of Microfabrication Techniques

Microfabrication is associated with the fabrication of microstructures based on lithography techniques with photolithography and soft lithography as flagship examples[77]. Here, photolithography and soft lithography methods will be briefly described below.

1.2.3.1 Photolithography

Photolithography, where light is used to pattern a substrate, is arguably the most common form of lithography[78]. This technique relies on transferring a pattern printed on a photomask, typically using UV light, onto a light-sensitive photoresist that has been previously deposited on a substrate[43,79]. Other lithography techniques for higher-resolution patterns include using x-rays, and ion or electron beams. The photoresist consists of a polymer, a sensitiser and solvent where each component has a specific function. The exposure of the polymer to radiation leads to changes in its structure. The solvent enables the photoresist to be spun and form thin layers on the substrate surface, and the sensitiser controls the photochemical reaction of the polymer upon exposure to radiation[80]. Briefly, a photolithography process starts by depositing the photoresist on a clean substrate *via* spin coating[78], with the spinning speed defining the thickness of the photeresist[43]. The substrate is then exposed to UV radiation to define a geometric pattern based on the design of the photomask[81]. The photomask typically consists of a glass or quartz plate with a chromium geometric pattern defined by computer-assisted design (CAD)[43]. The UV radiation can travel through the photomask via the unpatterned regions while being blocked by the patterned chromium design[78]. This is achieved by precise alignment of the photomask and substrate using a mask aligner[43]. Following a post-exposure bake, to promote the exposure-activated reaction, development using a solvent removes the unpatterned areas by dissolving the photoresist[43]. Positive photoresists are weakened when exposed to UV and thus become more soluble to the developer. For negative photoresists, exposure to UV induces photopolymerization and the unexposed areas are removed upon immersion into the developer[81]. Fabrication of high-resolution patterns can be accomplished by careful controlling the development time and the other fabrication parameters[43].

1.2.3.2 Soft lithography and Bonding

The fabrication of master moulds by photolithography allows the repeated fabrication of microfluidic devices by soft lithography. Repeated casting with an elastomer includes several advantages such as rapid prototyping and easy fabrication of microfluidic devices without the need of expensive equipment. The name soft lithography emerged from the use of elastomers[82,83]. For the fabrication of microfluidic devices, soft lithography begins where photolithography ends: with a master mould with a patterned structure. An elastomer is poured onto the master mould, cured, and de-moulded, transferring the pattern to the solidified elastomer[84]. The elastomer can then be bonded to glass or another elastomer layer, thus sealing the structures and completing the fabrication of a microfluidic device[85]. PDMS is considered the elastomer of preference for most soft lithography applications and can be bonded very well to glass or other PDMS layers. It is comprised by two components: a PDMS prepolymer and a curing agent. To initiate polymerisation the two parts must be mixed thoroughly at a weight ratio according to the manufacturer's instructions, degassed and poured onto the mould. The curing process generally occurs at an elevated temperature for a couple of hours to accelerate the cross-linking reaction. Then the PDMS microfluidic devices are peeled off from the mould with relief patterns in the PDMS as hollow channels[43,82].

Oxygen/air plasma is typically used to bond PDMS to glass or another PDMS layer enabling the construction of complex or multi-layered microfluidic devices[85]. This widespread process involves the oxidation of the substrates by creating hydroxyl groups at their surface followed by thermal support to promote the formation of covalent bonds[86]. The plasma oxidation of PDMS and glass results in charged surfaces that are energetically favourable to bonding. The methyl functional groups of PDMS are replaced by hydroxyl groups resulting in a silanol surface and the silicon dioxide of glass also forms silanol groups. The two oxidised surfaces (either glass-PDMS or PDMS-PDMS) are brought into contact and form silicon-oxygen-silicon (Si-O-Si) bonds at their interface leading to the formation of an irreversible bond[85]. The bonding is sufficiently powerful that the two substrates cannot be peeled apart without failure in the cohesion of the bulk PDMS[43]. The two substrates should be brought into contact as soon as possible following plasma oxidation so that both substrates do not recover their hydrophobicity and lose the capacity to form a stable bond[87].

1.3 Microfluidic-based *in vitro* models

1.3.1 Digestion

Miniaturised digestive systems have been developed to study the digestion of expensive molecules in small volumes, potentially enabling high-throughput studies. Marze et al. designed a microfluidic device capable of simulating gastrointestinal conditions to study the digestion of oil droplets coated with β-lactoglobulin in terms of lipolysis and solubilisation[88]. The authors used continuous flow to renew digestive juices and remove digestion products around the oil droplets leading to complete solubilisation of the digestion products. This miniaturised system proved to be a promising tool for studying the bioaccessibility of lipophilic molecules, a requirement for intestinal permeability studied in nutrition, pharmacology and toxicology[88]. More recently, De Haan et al. developed a microfluidic digestion system with three compartments: mouth, stomach and small intestine[89]. As proof-of-concept, the authors demonstrated the digestion of starch, casein and lactoferrin. The miniaturised system incorporates a continuous-flow mode that allows samples to be processed either continuously or in a pulsative multi-dose scheme. Each compartment integrates micromixers with arrays of staggered-herringbone grooves fabricated in the channel ceiling[89]. The grooves perturb laminar flow profiles allowing different fluid streams to fold onto one another over the cross-section of the microchannel[89,90]. Thus, samples are continuously mixed with artificial digestive juices containing enzymes, in physiologically relevant ratios providing faster enzymatic digestion throughout the gastrointestinal tract than in batchwise *in vitro* digestions[89].

1.3.2 Intestinal Permeability

Microfluidic, dynamic 3D models capable of mimicking the human intestine are advantageous because they allow continuous flow into both apical and basolateral chambers and thus replicate flow-derived shear stress. Continuous flow becomes an important parameter to ensure constant nutrient supply and waste product removal as well as the removal of exceeding bacterial growth allowing for long-term (up to 3 weeks) co-culture of commensal microbes. Some advances in gut-on-a-chip models incorporate peristaltic movements, which regulates cell differentiation, and the growth of microbiota without compromising human cell viability[91–95].

The first example of an intestinal model with integrated fluid flow was described by Brand and colleagues[96]. Caco-2 cells were cultured on a Transwell membrane with continuous flow on the basolateral chamber to study the diffusion of peroxovanadium and its effect on Hep-G2 liver cells. However, Caco-2 remained in static conditions[97]. Around the same time, Kimura et al. developed a PDMS-based device separated by a polyester semi-permeable membrane to address technical problems of long-term cultures

difficult to differentiate[98]. Caco-2 cells were cultured on the apical chamber and formed a functional monolayer, and the polarised transporter activity was monitored in real-time using an on-chip optical detection system[98]. The authors later described an on-chip small intestine-liver-lung coupled model intended to perform pharmacokinetics studies of anticancer drugs targeting the lung. Although the optimised system approximated more closely the cellular complexity found in these tissues, the real-time optical detection feature was omitted from this platform[99]. Imura et al. developed a similar on-chip intestinal model to evaluate the absorption of cyclophosphamide and Lucifer Yellow, chosen to represent a positive and negative control of intestinal absorption, respectively[100]. The same authors introduced a microsystem integrating a microintestine, microliver, and target cells to evaluate the intestinal absorption, hepatic metabolism and bioactivity of several chemicals.[101] The model was later improved to recapitulate the gastrointestinal digestion process that occurs before absorption at the small intestine[102]. Using a single platform, the authors demonstrated the potential of microfluidics to integrate a sequential digestion process that could not be mimicked in conventional transwell-based assays.

Work within Shuler's group proposed an *in vitro* platform, coined gastrointestinal tract micro cell culture analogue (GI-μCCA), with two chambers fabricated in PMMA to accommodate a collagen-coated semi-permeable polycarbonate membrane for intestinal cell culture. The platform was firstly cultured with Caco-2 cells[103] and then co-cultured with HT29-MTX to allow the formation of a mucous layer[17]. Before the assembly, both Caco-2 and HT29-MTX were seeded and expanded off-chip for 16 days. The μCCA has been coupled with multi-organ combinatorial systems to investigate the toxic effects of acetaminophen (APAP) on lung[103] (L2) and liver[17] (HepG2/C3A) cells, before and after subjecting APAP to an *in vitro* digestion using a chyme mimic prepared off-chip. The μCCA/liver model was also used to study the transport and toxicity of 50-nm carboxylated polystyrene nanoparticles (NPs) as a model for inert, negatively charged NPs.[104]. The platform was further improved to integrate on-chip Ag/AgCl electrodes to measure the TEER[105], however, the measurements were recorded manually using a commercial volt-ohm meter. Recently, the authors showed a μCCA model that used immortalised human intestinal epithelial cells (hIECs) from primary cultures co-cultured with human myofibroblasts from patient colonic biopsies[106]. The liver module was also improved by using a polymer scaffold to create a 3D tissue construct.[107] The authors claim that the hIECs were able to differentiate into enterocytes, enteroendocrine, goblet and Paneth-like cells. To the best knowledge, there are no advanced gut-on-chip platforms with higher cellular complexity.

The NutriChip[108] introduced an integrated microfluidic platform to study the activation of immune cells following the transfer and processing of nutrients across the epithelial layer (Figure 4A and B). It used two fluidic networks made out of PDMS to separate a confluent layer of Caco-2 from a co-culture of U927 monocytic cells. The microfluidic platform was designed and mounted on a prototype manifold to allow the introduction of different stimuli to both cell chambers (Figure 4A-B). A series of normally-closed valves operated by external pressure controlled the communication between the cells and a third chamber with functionalised magnetic beads designed to capture target cytokines (IL-6). Because of the optical transparency of NutriChip, IL-6 detection could be performed on-chip using a fluorescence microscope.

The Human-Microbial Crosstalk (HuMiX®) is a microfluidic platform designed to replicate the gastrointestinal tract in co-culture with commensal bacteria (Figure 4C). The device comprises three co-laminar microchannels – luminal microbial compartment, human epithelial cell culture, and a perfusion chamber – which are separated using microporous membranes coated with mucins and collagen[109]. Although the platform allowed the co-cultivation of human and microbial cells in a controlled manner, the experiments were maintained for limited periods of time (<24 hours).

Ingber's lab at the Wyss Institute in Harvard has been at the forefront of organ-on-chip technology including examples of the lung,[110] kidney,[111] bone marrow,[112] blood-brain barrier[113] and the gut. Introduced by Kim et al., the "Gut-Chip" integrates a functional polarised intestinal epithelial barrier with spontaneous formation of intestinal villi, continuous microfluidic flow, cyclic stretching of the cell culture membrane to mimic peristalsis and co-culture with a commensal bacterial strain (*Lactobacillus rhamnosus* GG) for extended periods of time (Figure 4D). The microdevice comprises two microfluidic channels separated by a 20-μm thick ECM-coated porous membrane. The device was made from PDMS to allow peristaltic-like movements actuated pneumatically by two hollow chambers that lined the whole length of the fluidic channels. The authors reported spontaneous differentiation of Caco-2 cells into a polarised intestinal epithelium when under shear stress applied by fluid flow (0.02 dyne·cm^{-1}) and cyclic strain (10 % mean cell strain, 0.15 Hz). The TEER was monitored off-line using a commercial volt-ohm meter coupled to Ag/AgCl electrode wires introduced through the fluidic tubing connections. Critically, Caco-2 and *Lactobacillus* co-culture was achieved without compromising the viability of the host-microbiome model. In fact, in the co-culture the TEER increased indicating enhanced epithelial barrier function.

Many improvements and applications of the "Gut Chip" have been reported over time. For example, Caco-2 cells have been differentiated to form physiologically relevant villus structures containing absorptive, enteroendocrine, goblet and Paneth cells under continuous fluidic flow and peristalsis-like movements.[114]

Other examples include, i) the co-culture of multiple commensal bacterial strains;[94,115] ii) the introduction of microvascular endothelial cells and human peripheral blood mononuclear cells (PBMCs) in the basolateral chamber to mimic the endothelium and study inflammatory activation;[94] iii) the study of enterovirus infection on the human intestinal epithelium,[116] iv) the integration of microscale oxygen sensors and a custom-made anaerobic chamber to enable the co-culture with anaerobic bacteria,[117] and the culture of biopsy-derived intestinal organoids[118].

Research in gut- and organ-on-chip devices remains highly active today with the number of publications increasing in recent years. Recent examples include intricate multiple-organ systems,[119] rapid-prototyping fabrication,[120] on-chip culture of full thickness intestinal sections,[121] and the development of membrane-free models using the fundamental properties of microfluidic laminar flow,[122] among others.[123,124]

Important challenges need to be solved within the development of reliable gut-on-chip platforms including the introduction of online barrier integrity monitoring systems, the ability to replicate in the same device the digestive process preceding absorption at the intestine and, high-resolution temporal profiling of epithelial barrier responses. However, it is clear that microfluidic platforms play an important role as *in vitro* models for drug and food development, contributing to accelerate the introduction and acceptance of a new generation of nanoformulated compounds.

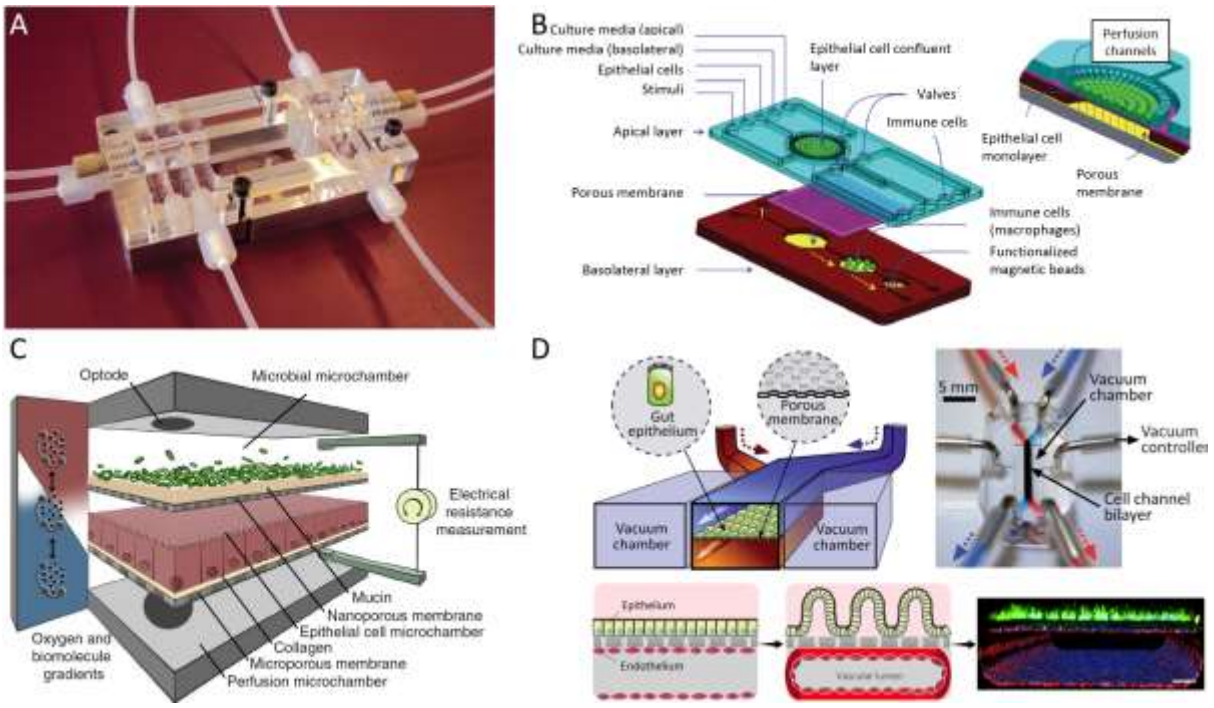

Figure 4. Microfluidic Gut-chip platforms. (A-B) The NutriChip developed at EPFL used multiple chambers to the activation of immune cells in response to the transfer and processing of nutrients across the epithelial cell layer. Image was adapted with permission from Ramadan et al.[108] C) HuMiX uses 3 parallel chambers separated by 2 microporous membranes to allow the co-culture of the intestinal epithelium with anaerobic bacteria [109]. D) The Gut-Chip from the Wyss Institute simulates peristalsis-like movements by the application of vacuum to two hollow chambers that line the whole length of the fluidic channels. Images adapted with permission from Kim et al.[95] and Firoozinezhad et al.[116]

2. Project Goals and Strategy

The present work is integrated in a FCT project, the MICRODIGEST project, that aims to fabricate a modular micro-device to mimic the complete gastrointestinal tract to predict the digestibility and bioaccessibility of orally administered active compounds. The proposed gastrointestinal tract-on-a-chip will recreate the physiological digestive conditions which include pH changes and enzymatic actions that may affect bioactive compounds in an independent module (digestion-chip). Furthermore, the project explores the fabrication of a cell-based module (gut-chip) including mechanical movements (peristalsis) and fluid flow, to be used as an alternative to simple/poor *in vitro* cell cultures (static cultures) to evaluate the intestinal permeability of digested samples. For this, microfluidic devices were fabricated from PDMS - chosen for its physical characteristics, such as optical transparency and gas permeability. However, the intrinsic hydrophobic property of PDMS can be problematic when studying small hydrophobic compounds. Thus, significant work within this thesis aimed to identify suitable coatings or surface treatments to reduce the absorption of small molecules by PDMS, thus allowing the validation of the modular micro-device. The following main aims were established:

1. Fabrication of modular microfluidic digestion-chip and gut-chip devices
2. Surface and bulk modification of PDMS microfluidic devices
3. Assessment of the PDMS modification through analytical methods
4. *In vitro* digestion: static versus on-chip
5. On-chip cell culture

3.Materials and Methods

3.1 Materials

Dow Corning Sylgard® 184 polydimethylsiloxane (PDMS) was purchased from Ellsworth Adhesives Ibérica (Madrid, Spain). TI prime, SU-8 2025 and SU-8 2100 were from MicroChem Corp. (Westborough, MA, USA). Nile Red, Rhodamine B, Fluorescein sodium salt, phosphate buffered saline (PBS), ethanol, acetone, Pluronic F-127, (3-aminopropyl)triethoxysilane (APTES), diisopropylamine, tetraethyl orthosilicate (TEOS), methylamine, dimethyl sulfoxide (DMSO), paraformaldehyde (PFA), phalloidin-tetramethyl isothiocyanate (phalloidin-TRITC), bovine serum albumin (BSA), fluoroshield™, sodium pyruvate solution 100 mM, resazurin sodium salt, Dulbecco's modified Eagle's Medium-high glucose (DMEM), pepsin from porcine gastric mucosa, bovine bile and pancreatin from porcine pancreas were obtained from Sigma-Aldrich (St. Louis, MO, USA). BODIPY TR-X casein, 4′, 6-diamidino-2-phenylindole, dilactate (DAPI, Invitrogen™), Matrigel™ membrane matrix, rat tail type-I collagen, Sulfo-SANPAH (sulfosuccinimidyl 6-(4'-azido-2'-nitrophenylamino)hexanoate) were obtained from Thermo Fisher Scientific (Waltham, MA, USA). Ethyl acetate was obtained from PubChem (Bethesda, MD, USA). Caco-2 cells were purchased from the American Type Culture Collection (ATCC®). Minimum essential media (MEM) Eagle was purchased from PAN-Biotech GmbH (Aidenbach, Germany). Millex-GS Syringe Filter Units 0.22, trypsin-EDTA (0.25% trypsin; 0.1% EDTA), penicillin/streptomycin 100x, foetal bovine serum (FBS) and 1-µm pore size transwell™ inserts were purchased from Merck Millipore (Burlington, MA, USA). 24 and 12-well plates were purchased from TPP Techno Plastic Products AG (Trasadingen, Switzerland).

3.2 Device Design

Devices were designed using CleWin4 from WieWeb Software (Hengelo, The Netherlands). The top PDMS slab of the Digestion-Chip included the staggering herringbone micromixers (SHMs) (19.5 half cycles of 6 grooves each). The grooves (50-µm wide) were set at a 45° angle to the main direction of flow, spaced evenly (100-µm pitch) and with the wide arms occupying 2/3 of the channel width. The channels were rectangular at 80-µm high (+ 20-µm from the SHMs) and 200-µm wide. The bottom PDMS slab contained two serpentine channels (500-µm high, 1-mm wide) to allow large incubation times of 2 h in each phase: gastric and intestinal. The top and bottom PDMS slab of the Gut-chip were 1 mm high by 1 mm wide and 200 µm high by 1 mm wide, respectively. The device designs can be visualised in Figure 5.

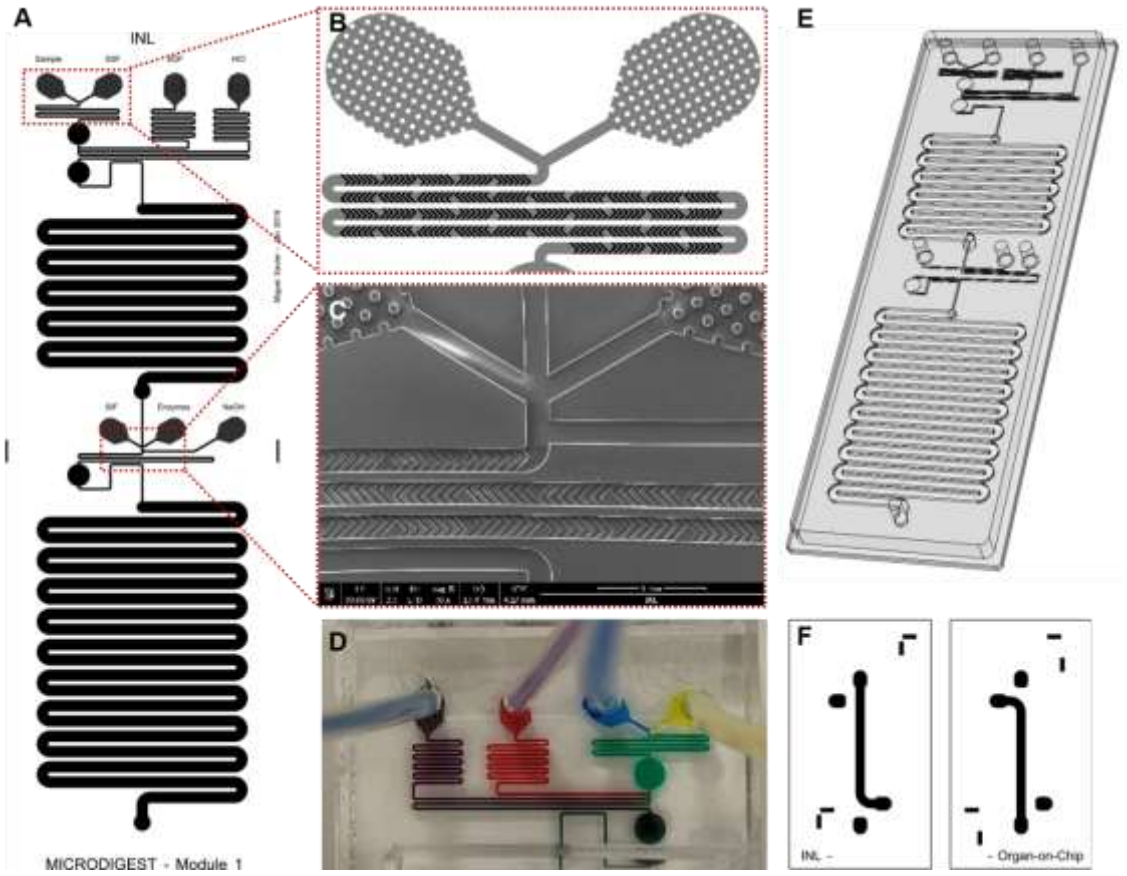

Figure 5. (A) Schematic representation of the digestion-chip design, (B) staggering herringbone micromixers (SHMs) to allow the mixing between the sample and the simulant salivary fluid, (C) SHMs to allow mixing of chyme and simulant intestinal fluid, (D) visualisation of the mixing seen by the colour change as the different dyes are being introduced in the SHMs (E) 3D representation of the digestion-chip and (F) gut-chip design (top and bottom slab).

3.3 Device Fabrication

3.3.1 Digestion-chip

Master moulds (Figure 6A and B) were manufactured on silicon wafers using a negative photoresist. Firstly, the substrate was cleaned with piranha solution (50% sulphuric acid, 50% hydrogen peroxide) and dehydrated overnight at 210 °C. The wafer was removed from the oven and cooled at room temperature before spin-coating of TI prime at 3,000 rpm for 30 s, as an adhesion promoter. SU-8 2100 or 2025 were then spin-coated for 30 s and soft baked before the exposure to UV radiation using a SUSS MicroTec MA6/BA6 mask aligner (Garching, Germany). Wafers were finally post-exposure baked and developed in propylene glycol monomethyl ether acetate (PGMEA) and hard baked. Details of the process specifications are detailed in Table 1. Master moulds were then treated with an anti-adhesion layer of trichloro(1H,1H,2H,2H-perfluorooctyl)silane, under vacuum, to facilitate the detachment of PDMS from the wafer. The Sylgard 184 PDMS pre-polymer and curing agent were weighed (10:1, w/w), degassed, poured over the master mould, and cured for 2 h at 65 °C. After curing, the PDMS was peeled away from the master mould and inlets and outlets were opened using a 1.5 mm diameter Kai Medical biopsy puncher. The two PDMS layers were oxygen plasma treated (Harrick Plasma Cleaner) for 30 s and brought into contact producing an irreversible bond (Si-O-Si) by condensation.

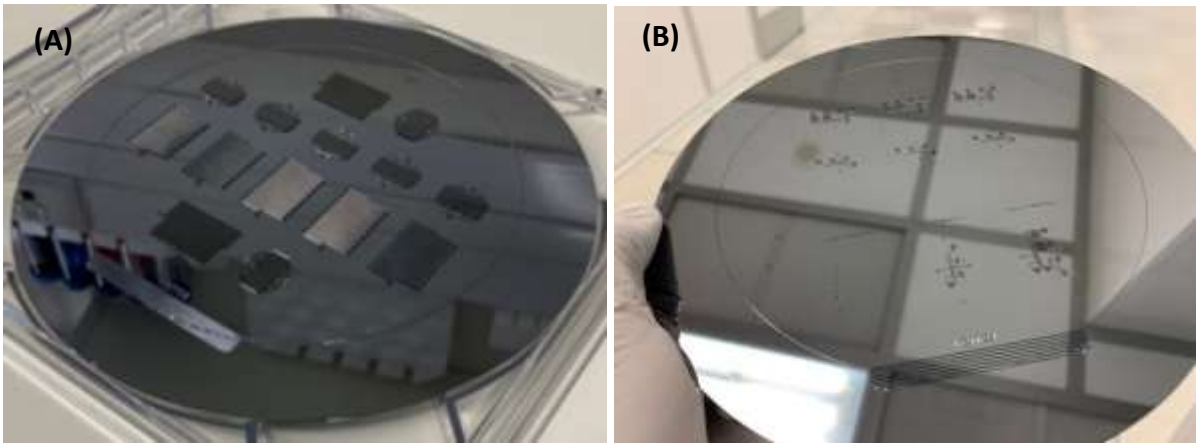

Figure 6. Fabrication of the digestion-chip. Silicon master mould of the (A) stomach and intestinal incubation compartments and (B) staggering herringbone micromixers.

Table 1. Microfabrication specifications for the fabrication of the silicon master moulds used for PDMS casting of the digestion-chip devices. Features with 20 and 80 μm were used to fabricate the staggering herringbone micromixers, 250 μm to fabricate the stomach compartment and 500 μm to fabricate the small intestine compartment.

Feature height	**20 μm**	**80 μm**	**250 μm**	**500 μm**
Photoresist	SU-8 2025	SU-8 2025	SU-8 2100	SU-8 2100
Spin-coating speed	4,000 rpm	1,000 rpm	1,100 rpm	1,100 rpm (2x)
Pre-exposure bake	65 °C, for 1 min. 95 °C, for 5 min.	65 °C, for 3 min 95 °C, for 9 min.	65 °C, for 7 min 95 °C, for 52 min.	65 °C, for 7 min. (2x) 95 °C, for 52 min. (2x)
Exposure dose	150 mJ·cm^{-2}	215 mJ·cm^{-2}	360 mJ·cm^{-2}	560 mJ·cm^{-2}
Post-exposure bake	65 °C, for 1 min. 95 °C, for 5 min.	65 °C, for 2 min 95 °C, for 7 min.	65 °C, for 5 min 95 °C, for 17.5 min	65 °C, for 5 min. 95 °C, for 28 min.
Development	4 min.	7 min.	18.5 min.	28 min.
Hard bake	150 °C, for 20 min.	150 °C, for 20 min	150 °C, for 20 min	150 °C, for 20 min.

3.3.2 Gut-chip

Master moulds were manufactured on PMMA using computer numerical control (CNC) machining (FlexiCAM Viper CNC, FlexiCAM GmbH, Eibelstadt, Germany). Gut-chips were assembled by O_2-plasma, bonding the bottom PDMS slab to a semi-permeable PDMS membrane fabricated in-house and placed in a dry oven for 15 min to permanently bond the membrane to the bottom layer and then cooled to room temperature. The PDMS membrane bonded to the bottom channel was carefully peeled away from the silicon master mould. Inlets and outlets were punched into the top PDMS slab using 1.5-mm diameter biopsy punchers. The bottom (plus membrane) and top channels were oxygen plasma treated and bonded under a magnifying lamp using an alignment rig built in-house, such that the channels and sidewalls of the top and bottom layers overlapped. The assembly was placed in the oven at 65 °C for 15 min to allow irreversible bonding.

3.3.2.1 PDMS Membrane

Silicon micropillar arrays (8-μm diameter, 32-μm pitch, 40-μm height, and offset every 2 rows - Figure 7), kindly fabricated by the INL cleanroom staff, were pre-treated with trichlorosilane in a vacuum desiccator overnight at 65 °C. Following silanisation, Sylgard 184 PDMS pre-polymer and curing agent were mixed at a 15:1 ratio (w/w), degassed, and poured over the silanised silicon master moulds placed on a spin coater. The PDMS was spread over the silicon master mould by spinning at 500 rpm for 20 s and then ramping up to 2400 rpm for 300 s. After spinning, the PDMS layer was allowed to rest on the silicon master moulds for an additional 10 min to allow the edge bead to retract. The spin-coated silicon master moulds were cured at 65 °C for 2 h and removed from the oven to cool down to room temperature.

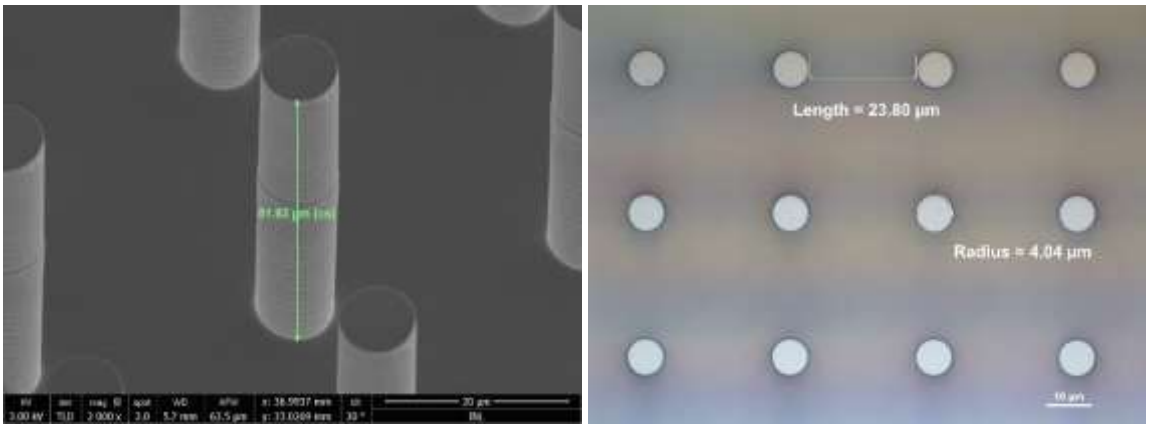

Figure 7. SEM images of silicon master moulds with micropillar arrays. Images were taken by the International Iberian Laboratory Nanotechnology (INL), Portugal, cleanroom staff.

3.4 PDMS Modification

3.4.1 Surface Modification

3.4.1.1 Pluronic F-127

PDMS devices were immersed in a 3% (w/v) Pluronic® F127 solution in 1x PBS for 24 h. To evaluate the effect of surface oxidation on the modification with Pluronic® F127, the same process was tested in cured PDMS devices used untreated and following oxygen plasma treatment.

3.4.1.2 (3-Aminopropyl)triethoxysilane (APTES)

PDMS devices were cured at 80 °C for 1 h and oxygen plasma treated for 30 s. Immediately, the oxidised surface was immersed in a freshly prepared 1 or 10% APTES solution in a 50:50 (v:v) water and ethanol mixture to promote the formation of a covalent bond between the APTES molecules and the PDMS surface. The devices were finally washed with diH_2O and dried under a stream of nitrogen.

3.4.2 Bulk Modification of PDMS

3.4.2.1 Gradient-Induced Migration of Embedded Pluronic

Gradient-induced migration of embedded poloxamers was done according to the methods described by Wu *et al.*[126] Briefly, a 200 mg/mL Pluronic® F-127 solution in ethanol was added to uncured PDMS at a 0.2% ratio (v/w), mixed thoroughly and cured for 1 h at 75 °C. The samples were then oxygen plasma treated for 30 s, incubated in a dry oven at 75 °C for further 30 min and immersed in diH_2O for 24 h.

3.4.2.2 Thermal Aging

PMDS thermal aging was done following the procedure reported by Eddington *et al.*[127] Briefly, PDMS devices were placed in a dry oven at 100 °C for 7 and 14 days to promote the volatilisation and removal of low molecular weight PDMS chains from the polymer matrix and oxidised by oxygen plasma.

3.4.2.3 Extraction of Uncrosslinked Contaminants using Organic Solvents

Uncrosslinked PDMS contaminants were extracted from the elastomer bulk by immersing the cured elastomer in an extremely soluble solvent followed by cycles of decreasing solubility as proposed by the Whitesides group[74] Briefly, PDMS devices were immersed in 150 mL of diisopropylamine for 1 day, transferred to 150 mL of ethyl acetate for a further day, and then to 300 mL of acetone for 2 days (with acetone renewed after 1 day). The samples were finally dried in an oven at 100 °C for 2 days and oxidised using oxygen plasma for 30 s.

3.4.2.4 Sol-Gel Treatment

PDMS modification using sol-gel chemistry was done according to the procedure described within Quake's group[128]. PDMS samples were cured at 80 °C for 1 h and immersed in TEOS in a glass container for 60 min. The samples were constantly stirred for the first 5 min to avoid attaching to the glass surface. The samples were then washed with pure ethanol to prevent the formation of silica crystals, rinsed with diH_2O, and immersed in a 4% (v/v) methylamine/water solution for 15 h. Methylamine and other contaminants introduced by the sol-gel treatment were eliminated from the bulk by immersion in diH_2O for 24 h (changing the water twice), which has been shown to improve biocompatibility of the resulting elastomer [128]. Finally, the samples were dried at 80-95 °C for 1 h and bonded to a glass slide using oxygen plasma.

3.5 Absorption Study

The long microfluidic serpentine channel was used for the absorption studies. Syringes containing the test solutions were connected to the devices using 1.6-mm outer diameter PTFE tubing and flow was driven by a New Era NE-2000 syringe pump (New Era Pump Systems, Inc., NY, USA). The solutions were collected from the outlet into an empty syringe to avoid solvent evaporation, and then analysed using a fluorescence BioTeK® Synergy H1 (Winnoski, VT, USA) microplate reader. Absorption was estimated by the fluorescence intensity ratio of the solutions before and after passage through the PDMS device. The excitation and emission maxima of Nile Red in ethanol (λ_{ex}: 543 nm; λ_{em}: 627 nm), Nile Red in ethanol/PBS (λ_{ex}: 584 nm; λ_{em}: 650 nm); fluorescein (λ_{ex}: 485 nm; λ_{em}: 515 nm) and rhodamine B (λ_{ex}: 550 nm; λ_{em}: 580 nm) were determined using a FluoroMax-4 spectrofluorometer from Horiba (Kyoto, Japan) (Figure S1).

The absorption of fluorescent molecules by the PDMS matrix was visualised and semi-quantified by a laser scanning confocal microscope (LSCM) (Zeiss LSM780; Oberkochen, Germany) using a 10x objective. A 488-nm and 513-nm argon lasers were used to image fluorescein and rhodamine B, respectively, while Nile red and BODIPY T-RX were imaged at 651 nm using a diode-pumped solid-state laser. The images were taken at multiple focal planes defined within the limits of each channel wall analysed using Zen 2010 software from Zeiss and ImageJ (Figure 8).

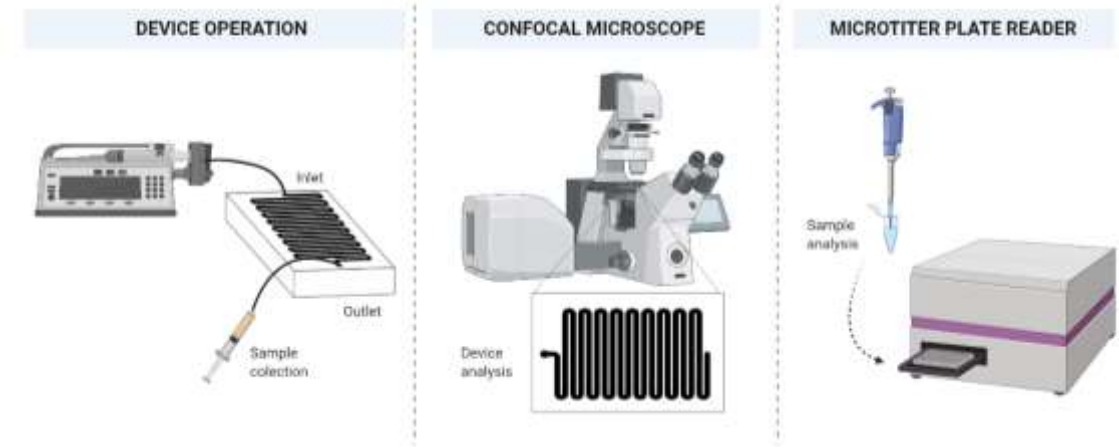

Figure 8. Schematic representation of the device operation. Created with Biorender.

3.6 Contact Angle Measurements

The water contact angle was measured using a Krüss Drop Shape Analyser - DSA 100 (Krüss GmbH, Hamburg, Germany). Following the conventional sessile drop method, a 5-µL drop of diH_2O was dispensed from a motor-driven syringe on the sample surface. The shape of each droplet was recorded using an integrated camera and the water contact angle value determined using DSA3 software. For each sample, the water contact angle was measured in three distinct locations to avoid the analysis of a pre-wetted surface.

3.7 *In Vitro* Digestion

Casein labelled with a pH-insensitive red fluorescent BODIPY TR-X dye was digested under simulation of gastrointestinal conditions based on the INFOGEST standardised protocol. This digestion reporter molecule is almost totally quenched when undigested. After exposure to enzymes during the digestion process, hydrolysis takes place releasing highly fluorescent dye-labeled peptides increasing the fluorescence intensity which is proportional to the extension of digestion. Throughout the *in vitro* digestion, the substrate was protected from light to avoid photobleaching. For digestion, the simulated salivary, gastric, and intestinal fluids were prepared following Table 2.

Table 2. Volumes of electrolyte stock solutions of simulated digestion fluids for a volume of 400 mL diluted with water (1.25× concentrated). Owing to the gas permeability of PDMS, both static and digestion-chip were performed considering as open systems. Following the recommendations of Brodkorb et al.[129], sodium bicarbonate ($NaHCO_3$) was replaced with NaCl at the same molar ratio to ensure the ionic strength of the electrolyte solutions (oral, gastric and intestinal) which was proven to be effective in avoiding undesirable pH drift. Important to note that the $CaCl_2(H_2O)_2$, pepsin, pancreatin and bile salts were added immediately before the experiment.

			Simulated Salivary Fluid (pH 7.0)		**Simulated Gastric Fluid (pH 3.0)**		**Simulated Intestinal Fluid (pH 7.0)**	
Salt solution added	Stock concentrations		Volume added to prepare 400 mL (1.25x)	Final salt concentration in SSF	Volume added to prepare 400 mL (1.25x)	Final salt concentration in SGF	Volume added to prepare 400 mL (1.25x)	Final salt concentration in SIF
	(g/L)	(M)	(mL)	(mM)	(mL)	(mM)	(mL)	(mM)
KCl	37.3	0.5	15.1	15.1	6.9	6.9	6.8	6.8
KH_2PO_4	68	0.5	3.7	3.7	0.9	0.9	0.8	0.8
NaCl	58.44	1	6.8	13.6	12.5	25	42.5	85
NaCl	117	2	-	-	11.8	47.2	9.6	38.4
$MgCl_2(H_2O)_6$	30.5	0.15	0.5	0.15	0.4	0.1	1.1	0.33
$(NH_4)_2CO_3$	48	0.5	0.06	0.06	0.5	0.5	-	-

3.7.1 Static Digestion

The simulation of the oral phase started by the addition of 5 mL of casein to a centrifuge tube with 4 mL of simulated salivary fluid (SSF), 25 µL of $CaCl_2(H_2O)_2$ and 975 µL of Milli-Q water. The mixture was placed in a thermomixer (Eppendorf™, Hamburg, Germany) at 37°C with constant shaking for 2 min to mimic the physiological conditions of the oral compartment. Then 7.76 mL of simulated gastric fluid (SGF) was combined with 970 µL pepsin (2,000 $U \cdot m^{-1}$) and 4.85 µL of $CaCl_2(H_2O)_2$ and added to the bolus. The pH was adjusted to 3.0 with 1M HCl and the reaction volume completed to 9.7 mL with Milli-Q water. The sample was maintained under constant shaking at 37°C for 120 min to simulate the stomach conditions. For the intestinal phase, 6.545 µL of simulated intestinal fluid (SIF), 2.805 µL of bile, 4.25 µL of $CaCl_2(H_2O)_2$ and 4.250 µL of pancreatin (100 $U \cdot mL^{-1}$) were added to the chyme and the pH adjusted with NaOH (1M) to 7.0. Finally, the mixture was completed with Milli-Q water to achieve a total volume of 17.0 mL and incubated under continuous shaking for another 120 min at 37°C. 300 µL of the digested sample were collected at the end of the oral digestion and during the gastric and small intestine digestion at each 15 min to measure fluorescence, using a microtiter plate reader.

3.7.2 On-chip Digestion

The microfluidic gastrointestinal model consists of three compartments which comprise the mouth, stomach, and small intestine. The sample and simulated digestion fluids were introduced through 1.6-mm outer diameter (OD) PTFE tubing connected to syringe pump-driven syringes at pre-set flow rates. Flow from the outlet was collected by another piece of PTFE tubing into a microcentrifuge tube. The flow rates used provided a mixing ratio of 1:1 between the substrate and artificial fluids, at each phase. When the digested sample reached the end of the microfluidic channel, 100 µL were collected onto the microcentrifuge tube in an ice bath to stop the reaction and the fluorescence measured using a microtiter plate reader. The incubation times were controlled according to the infusion flow rates considering the volumes of the gastric (96 µL) and intestinal incubation compartments (192 µL).

3.7.3 Mixing by Chaotic Advection

The mixing efficiency promoted by the staggered herringbone mixers (SHMs) was evaluated by flowing a 0 µM and a 5 µM sodium fluorescein solutions in diH_2O, in separate streams filling opposite halves of the cross section of the channel. The mixing in the channel was characterised through a 10x objective, using a confocal microscope equipped with a 488-nm argon laser.

3.8 Gut Chip Culture

3.8.1 Cell Culture

Caco-2 cells, from human colon adenocarcinoma, were routinely maintained in minimum essential media (MEM) supplemented with 20% FBS, 1% sodium pyruvate, 100 U·mL^{-1} of penicillin and 100 µg·mL^{-1} of streptomycin (1% Pen/Strep). Cells were maintained in a humidified chamber at 37 °C and 5% CO_2 atmosphere. Culture media was replenished every 2-3 days and cells were routinely sub-cultured at a maximum confluence of 70-80%. Adherent cells were detach using trypsin-EDTA for 5 min.

3.8.2 Cell Seeding On-chip

Gut-chips were sterilised by introducing 70% (v/v) ethanol through the microchannels for 30 min following a perfusion with PBS. Thereafter, sulfosuccinimidyl 6-(4'-azido-2'-nitrophenylamino)hexanoate (sulfo-SANPAH) (0.5 µg·mL^{-1}) in diH_2O was introduced through the upper microchannel and photo-activated by UV radiation (λ=365 nm; 6.8 W; distance: 5 cm) for 30 min to allow cell-surface protein crosslinking. The sulfo-SANPAH solution was removed from the microchannel and washed with sterile diH_2O, followed by cold PBS. An extracellular matrix (ECM) solution containing rat type I collagen (30 µg·mL^{-1}) and Matrigel (100 µg·mL^{-1}) in serum-free DMEM was added into the upper microchannel and incubated overnight at 4

°C, followed by 1 h at 37 °C, the day after. The ECM solution was removed from the upper channel and washed with serum-free media to remove ECM in excess.

Caco-2 cells were harvested, counted and seeded into the upper microchannel at 1 x 10^5 cells cm^{-2}. Cells were incubated overnight at 37 °C to allow their attachment to the ECM-coated PDMS surface. The following day, the devices were mounted on a home-built microscope and connected to a syringe pump using 1.6 mm OD PTFE tubing to perfuse culture medium continuously through the upper and lower microchannels at a constant flow rate (30 $\mu L \cdot h^{-1}$).

Static cultures of Caco-2 cells in Transwell inserts containing porous polyester membrane inserts (1.12 cm^2, 1-µm pores) were used as a control. Caco-2 cells were seeded at 1.0 x 10^5 cells cm^{-2} and the medium routinely changed every 2-3 days.

3.8.3 Immunocytochemistry

Cells were fixed with 4% (w/v) paraformaldehyde for 15 min and permeabilised by incubation with a 0.2% (v/v) Triton X-100 solution in PBS for 10 min. The fixed cells were incubated with a 2% (w/v) BSA solution in PBS (blocking solution) to minimise non-specific antibody bonding. After blocking, cells were incubated with 5 $\mu g \cdot mL^{-1}$ Alexa Fluor® 488 conjugated occludin monoclonal antibody (OC-3F10) and 0.1 $\mu g \cdot mL^{-1}$ phalloidin-TRITC overnight, at 4°C. After extensive washing, cells were stained with 1 $\mu g \cdot mL^{-1}$ DAPI for 10 min and preserved in fluoroshield mounting media. Images were taken using a confocal microscope equipped with 405-nm and 561-nm diode lasers and a 488-nm argon laser and analysed using Zen 2010 software and ImageJ.

3.9 Statistical Analysis

Results are shown as mean ± standard deviation. The Shapiro-Wilk test was used to confirm if data followed a normal distribution. P-values were determined using a two-way analysis of variance (ANOVA) with Tukey's post-hoc test or the Student's t-test for independent samples. All sample data analysis was performed using Graph Pad Prism 8.3.1 (San Diego, CA, USA).

4. Results and Discussion

4.1 Absorption studies

It is well established that PDMS works efficiently as a solid solvent[126].This capacity of PDMS to absorb mostly small molecules can be used to the benefit of the user but it is more often detrimental, as solution concentrations can be significantly altered leading to unpredictable alterations in experimental outcomes. To understand the dependence of this behaviour on various factors, such as nature of the solute/solvent, concentration and time, a series of experiments were conducted aiming to determine the conditions where molecule partition into PDMS could be problematic for certain study designs.

4.1.1 Molecule partitioning as a function of solute/solvent pairings

To study the absorption of different small molecules by PDMS, Nile Red, Rhodamine B and Fluorescein solutions were flowed through a serpentine microfluidic channel and the fluorescence of the solution was quantified by spectrophotometry before and after passage through the device. Direct absorption of the fluorophore into the PDMS channel walls was also semi-quantified by confocal microscopy images directly on-chip. These molecules were chosen for having different hydrophilicity, with octanol-water partition coefficients (K_{OW}) at 5.00, 2.74 and -0.67, respectively[130]. In addition, Nile Red was flowed diluted in either ethanol or in a 1:3 ethanol/PBS solution to determine the solute/solvent pairings effect on PDMS absorption. Importantly, PBS as a solvent represents a scenario that is more physiologically relevant and more likely to be used in biological studies.

Analysis of confocal microscopy images of the PDMS channel walls during passage of the three test solutions showed clearly that the partitioning of molecules into the PDMS matrix increased with the molecule K_{OW}. Channels where the Nile Red solution was flowed appear significantly more fluorescent (Figure 9). The strong interaction of PDMS with Nile Red can be related to a previous study carried out by Toepke and Beebe[75]. The authors also found continuous absorption of Nile Red after successive filling steps with 1 μM Nile red through a PDMS channel, indicating the accumulation of the fluorescent compound. Importantly, it should be noted that when the fluorescence of the solution collected at the outlet over the solution fed to the device was quantified, by spectrophotometry, there was actually an increase in the fluorescence intensity of the solution (Figure 10). This was due to solvent evaporation during the prolonged experimental times (up to 150 min), which was verified in a control experiment (Table 3). Critically, this shows the importance of using complementary methods in most experimental setups.



Figure 9. Confocal microscopy images of (A) 1 μM Nile Red, (B) 1 μM Rhodamine B and (C) 1 μM Fluorescein absorption into a PDMS channel wall at 96 μL·h^{-1}. Each image represents one slice of a z-stack taken over a 1.5 mm-high section of the PDMS channel and acquired at 50 μm increments.

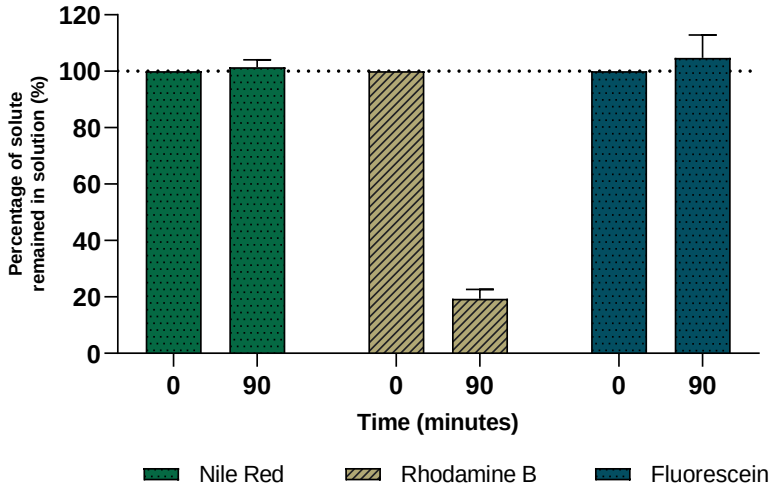

Figure 10. Percentage (%) of 1 μM Nile Red in ethanol and Rhodamine B and Fluorescein in PBS remained in solution after 90 min flowing through the PDMS microfluidic channel at 96 μL·h^{-1}. Values show mean and standard deviation of three independent experiments.

Table 3. Evaporation (%) of ethanol (density 0.789 g/mL) while flowing through the microfluidic channel for 150 min at 96 μL·h^{-1}.

	Expected Weight (mg)	Weight (mg)	Evaporation (%)
Sample 1	240	196	14
Sample 2	240	196	14
Sample 3	240	224	22
Sample 4	240	203	11
Mean ± SD	-	205 ± 13	15 ± 5

Nile Red is hydrophobic and thus is stable in ethanol[131], which contains polar (OH) and nonpolar (C_2H_5) terminals. When the Nile Red solution in ethanol was diluted 1:3 in PBS and flowed through the microchannel a significant increase in molecule partitioning was observed (Figure 11). Crucially, partitioning in these conditions was so significant that Nile Red was all absorbed at the inlet before it could be imaged in the device by microscopy. This points out the importance of considering solute/solvent pairings in studies using PDMS-based devices. For example, Nile Red is commonly used as a fluorescent marker in nanoemulsions[132]. While the molecule is stable in oil, digestion studies in a PDMS-based device leading to the release of Nile Red into the simulant digestion fluids, which are all aqueous based, would result in complete Nile Red absorption by the PDMS matrix thus significantly altering results interpretation.

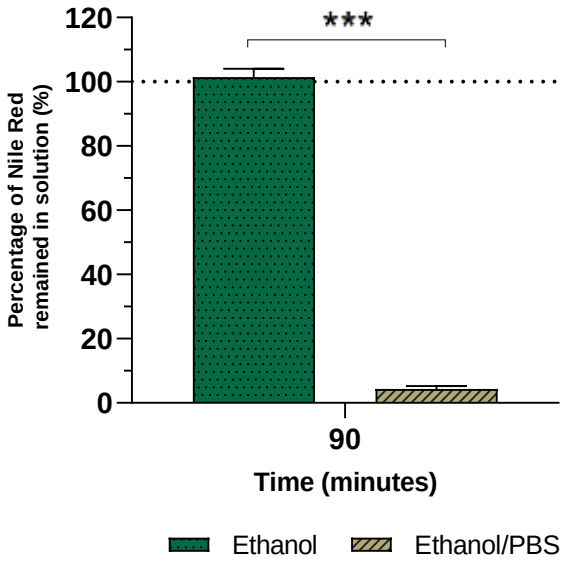

Figure 11. Nile Red absorption by PDMS as a function of the solvent used. Percentage (%) of Nile red remained in solution after flowing 1 µM Nile red in ethanol or 0.3 µM in ethanol/PBS through the microfluidic device for 90 min at 96 µL·h^{-1}. Values show the mean and standard deviation of three independent experiments; ***p < 0.001 with p-values obtained using the Student's t-test that followed a normal distribution according to the Shapiro-Wilk test.

4.1.2 Molecule partitioning as a function of residence time

Another factor affecting molecule partitioning into the PDMS matrix is residence time. In the examples above, particularly long experimental times were used, which are relevant for digestion-on-chip applications – one of the subjects of this thesis – but not common in the majority of microfluidic applications where small channel dimensions and high-throughput typically imply short residence times inside devices. 1 µM Nile Red solution in Ethanol/PBS (1:3 ratio) was flowed through the device at 400 µL·h^{-1} or at 1,000 µL·h^{-1}. Figure 12 shows that the amount of Nile Red that remained in solution was significantly higher (29.9 *vs* 11.8 %) when the flow rate was 1,000 µL·h^{-1}.

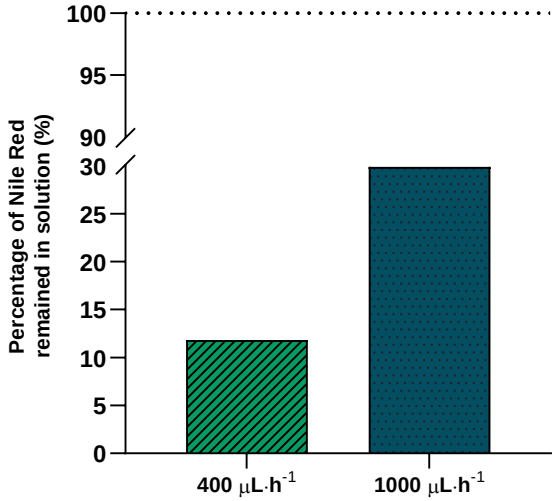

Figure 12. Nile Red absorption by PDMS as a function of the residence time. Percentage (%) of Nile Red remained in solution after the first passage of Nile red in ethanol/PBS (1:3 ratio) through the microfluidic channel at a flow rate of 400 μL·h^{-1} and 1000 μL·h^{-1}. Values show the measurement of one independent experiment.

4.1.3 Molecule partitioning as a function of concentration

It is intuitive that higher solute concentrations should lead to higher absorption by PDMS as a greater concentration gradient is formed. Figure 13 shows that when 20 μM rhodamine B in PBS was flowed through the device there was a significantly higher absorption of the fluorophore to the PDMS matrix, when compared to a 1 μM solution. Importantly though, in relative terms the percentage of solute that remained in solution was higher for the 20 μM solution where a relative reduction of just under 20% in concentration was observed, contrasting with nearly 100% for the 1 μM solution after the first passage. (Figure 14). This indicates that although more solute is absorbed by PDMS at higher concentrations, in fact it is at minute concentrations that molecule partitioning into the PDMS matrix is particularly notable. This is critical given that at low concentrations, solutes are often close to the limits of detection of analytical methods. Thus, such reductions in concentration could lead to complete failure to detect the formation of fluorescent species in on-chip reactions. Interestingly, at later time-points (>120 min) the relative concentration of rhodamine B in the output solution increases, initially to just 4% over the initial concentration at the inlet, but later up to nearly 30%. This suggests that as the PDMS matrix becomes saturated with rhodamine B, a lower uptake from the solution is observed.

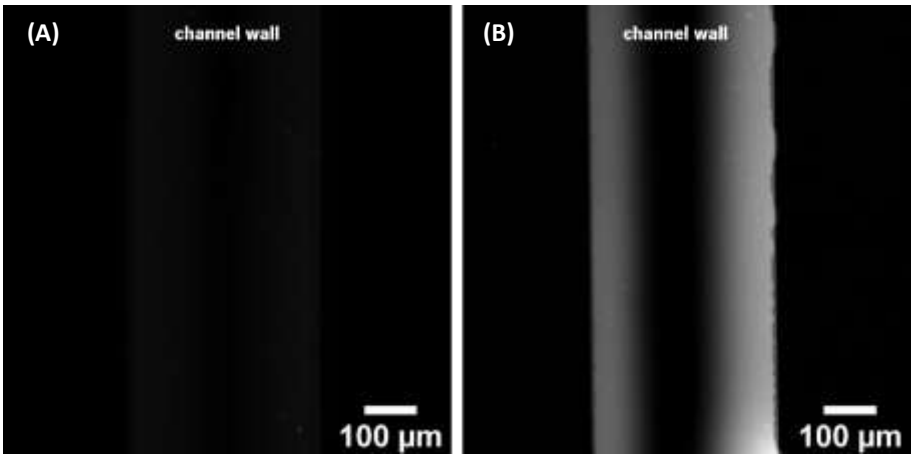

Figure 13. Confocal images showing the absorption of Rhodamine B into the PDMS channel wall after the flow of (A) 1 µM and (B) 20 µM solutions.

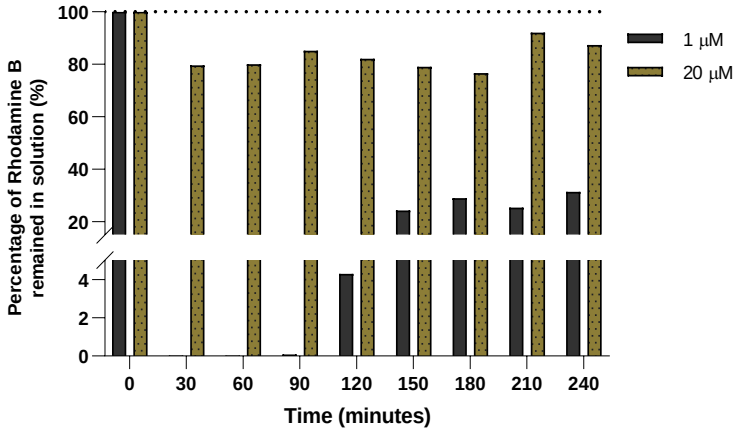

Figure 14. Rhodamine B absorption by PDMS as a function of concentration. Percentage (%) of Rhodamine B remained in solution after flowing 1 µM or 20 µM rhodamine B at 400 $\mu L \cdot h^{-1}$ collecting a sample every 30 min. Values show the measurement of one independent experiment.

4.2 PDMS modification aiming to reduce molecules absorption

4.2.1 Water contact angle studies

Aiming to reduce the absorption of small molecules by PDMS, a series of surface and bulk modifications found in the current literature were tested and compared. To verify the extent and stability of the modifications, the water contact angle (CA) of the PDMS surface was monitored over time (up to 21 days). PDMS is a hydrophobic elastomer[133] presenting a CA around 110°. Theoretically a reduction of the water CA should lead to a lower tendency for absorbing small hydrophobic molecules (*e.g.* Nile Red).

Figure 15 shows that all the modifications tested, except for a surface modification with Pluronic-F127 (P-F127), led to a sharp decrease of the surface contact angle of PDMS, in some cases to values as low as 10°. However, there was equally a general tendency for the CA to return to values rounding 100° over time. This tendency was more or less marked depending on the modification, with an oxygen plasma treatment quickly followed by immersion in P-F127 appearing to produce the most stable modification, where the CA remained under 50° for a whole week, increasing to 75° after 3 weeks. This reversion of PDMS to its original surface properties has been documented[74,126,127] and can be justified by the reorientation of polar groups from the surface into the bulk, or the migration of uncrosslinked PDMS oligomers from the bulk to the surface.

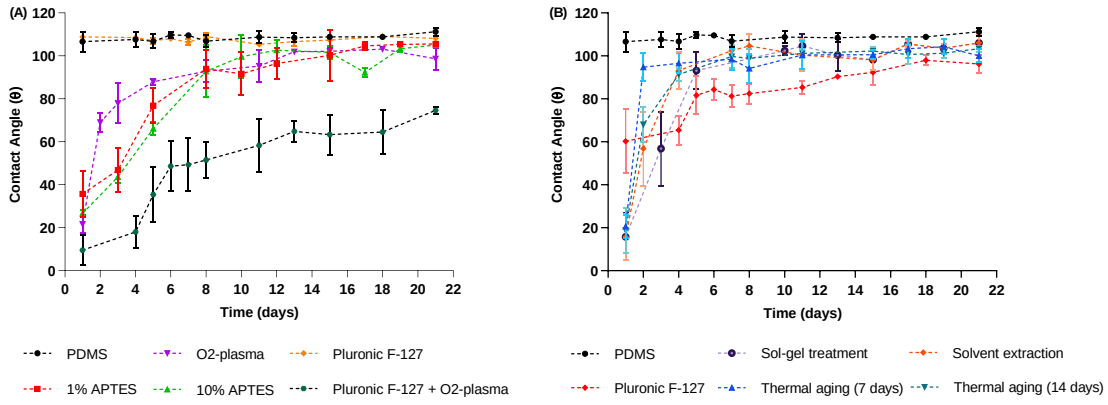

Figure 15. Relation of the water contact measurements as a function of time of (A) surface and (B) bulk modified PDMS. Values show mean and standard deviations from at least 3 independent measurements.

4.2.2 Absorption studies

Although none of the modifications tested led to a stable reduction of the surface CA of PDMS, some achieved a significant reduction up to 7 days after treatment. Thus, the absorption of Nile Red in an ethanol/PBS (1:3 ratio) solution was compared between unmodified PDMS and some of the best-performing modifications in terms of CA reduction.

Figures 16 show that although the modifications led to a transient decrease in the surface CA, these did not translate into lower partitioning of Nile Red into the PDMS matrix. Indeed, some modifications led to a significant increase ($p<0.01$) in the absorption of Nile Red into the PDMS bulk (*e.g.,* solvent extraction and 14-day thermal aging). This indicates that the absorption of small molecules by PDMS is likely less affected by its surface chemistry than it is by its highly porous structure[134]. Indeed, although the bulk modification with TEOS by sol-gel treatment aiming to fill the PDMS matrix with silica particles also did not lead to a reduction in Nile Red absorption, it significantly impaired the diffusion of Rhodamine B into the polymer matrix (Figure 17) which was in agreement with the work by Gomez-Sjoberg et al.[128]

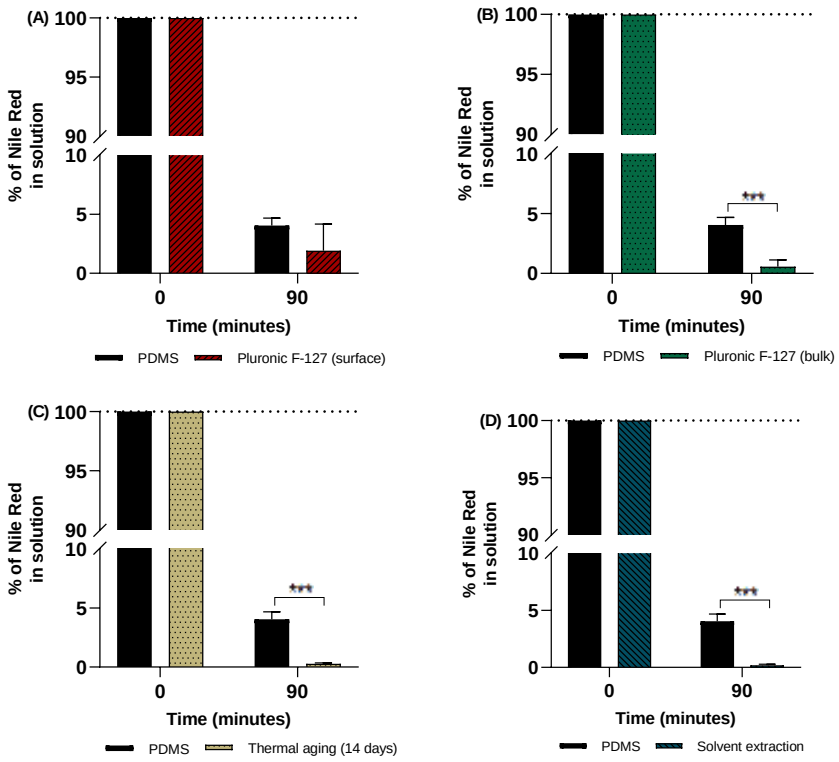

Figure 16. Percentage (%) of Nile Red remained in solution after flowing 1 µM Nile Red in ethanol/PBS (1:3 ratio) on unmodified PDMS, (A) PDMS surface modified with 3% Pluronic F-127, (B) PDMS bulk modified with Pluronic F-127, (C) PDMS modified with 14 days of thermal aging and (D) PDMS modified with organic solvents. Values show mean and standard deviation from a minimum of two independent experiments; ***$p < 0.01$, p-values obtained using a two-way analysis of variance (ANOVA) with Tukey's post-hoc test.

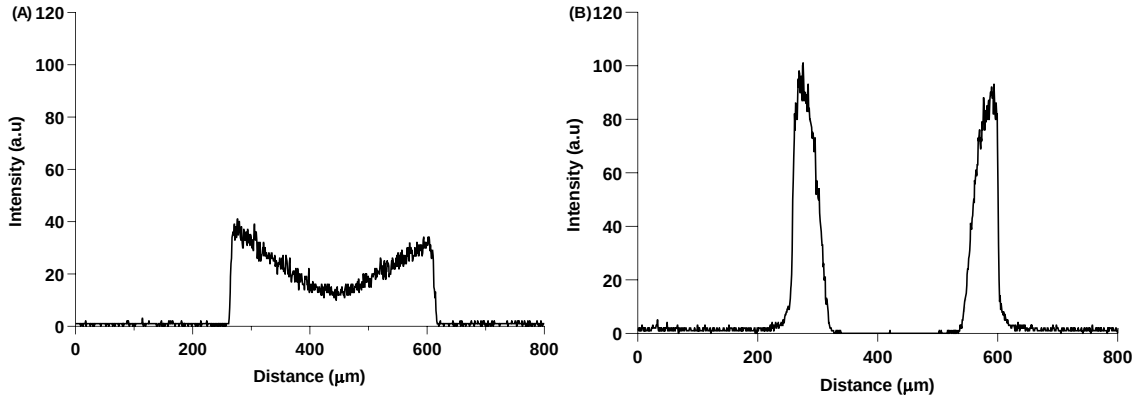

Figure 17. Fluorescence intensity profiles obtained from the confocal micrographs after flowing 20 μM Rhodamine B on (A) unmodified PDMS and (B) bulk modified PDMS with sol-gel treatment. These line profiles were acquired after 240 min of flow at 400 $\mu L \cdot h^{-1}$.

In conclusion, this study reiterated the capacity of PDMS to work as an efficient solid solvent. While this property may be used to the benefit of the user, it will more often be detrimental, particularly in applications where precise quantification of an analyte is required. Whether the absorption of molecules of interest by PDMS may pose a problem, it should be assessed on a case-by-case basis as this will depend on a variety of factors including the nature of the molecule, the solvent, residence time and the concentrations used. The PDMS surface and bulk treatments tested here, although leading to a transient increase in the hydrophilicity of the elastomer, did not produce any significant reduction of the absorption of the test molecule Nile Red. Thus, where molecule absorption is deemed to be problematic, alternative materials to PDMS should be considered for device fabrication.

4.3 On-chip *in vitro* digestion

As proof-of-concept and to allow direct comparison between the static *in vitro* and on-chip digestions, a quenched, fluorescently-labelled casein derivative (EnzCheck™ Protease Assay Kit, ThermoFisher) was used as test molecule. The dye is quenched by proximity but becomes fluorescent upon hydrolysis, thus working as a digestion reporter molecule to determine protease activity. Considering the issues related with the absorption of small molecules by PDMS, first it was important to verify whether the hydrolysed casein (reporter) would be significantly absorbed by PDMS. For this, casein was digested off-chip and then flowed through the digestion-chip for 300 min. The fluorescence was measured before and after flowing through the device and a reduction of 13% in relative fluorescence intensity was observed (Figure 18) which was considered acceptable.

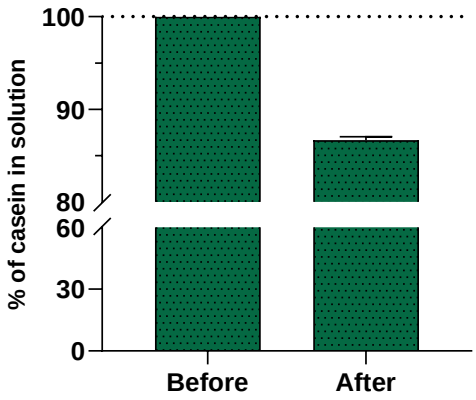

Figure 18. Percentage (%) of digested casein remained in solution after flowing through the digestion-chip for 300 min at 96 $\mu L \cdot h^{-1}$. Values show the mean and standard deviation of three samples of one independent experiment.

4.3.1 Mixing by chaotic advection

In the digestion-chip, the flow followed the Stokes' or laminar regimes with Reynolds values (Table S1) ranging from $4x10^{-2}$ to 4.25 at the range of flow rates used (0.024 - 2.3 mL·h^{-1}). Here, the laminar flow contributes to a mixing solely based on diffusion mechanism which can add a drawback to digestions. Thus, a staggered herringbone mixer (SHM), first introduced by Stroock *et al.*[90], was incorporated following each channel junction in the device to promote mixing by chaotic advection. Figure 19 shows complete mixing of water (0 µM) and a 5 µM sodium fluorescein solutions in diH_2O in the SHM, after 7.5 cycles at 2.3 mL·h^{-1}. Decreasing the flow rate would indicate a complete mixing sooner allowing diffusion to occur for longer periods of time. Considering these conditions, a complete mixing of samples and digestion fluids before reaching the incubation compartments was ensured in every experimental condition of the present study.

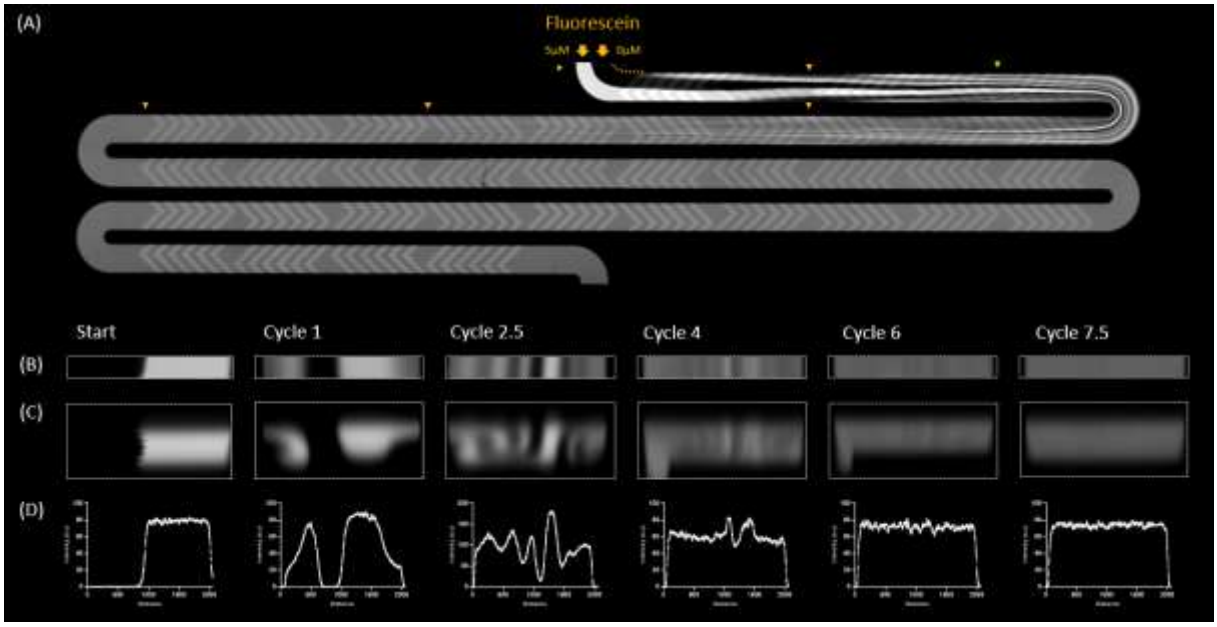

Figure 19. Performance of the mixing process in micromixers with herringbone-shaped grooves. (A) Confocal micrograph of fluorescein (5 µM in water) being continuously mixed with water (0 µM) as the mixing proceeds along the microchannel. (B-C) Top and orthogonal cross-section views of the fluorescence intensity distribution upstream of the features, respectively. (D) Fluorescence intensity profiles extrapolated from cross sections after one cycle, two half cycle, four cycles, six cycles and seven half cycles.

4.3.2 Enzyme kinetics

To study enzymatic kinetics, casein was diluted in different concentrations [S] (2-100 μg·mL^{-1}) and mixed off-chip with SSF to represent the output of the oral digestion phase. The prepared bolus and SGF (2,000 U·mL^{-1} pepsin) were introduced in separated inlets at 1152 μL·h^{-1} and flowed through a SHM for mixing and then to a long serpentine channel for incubation. Here, the total incubation time in the serpentine channel was 220 s at 2.3 mL·h^{-1}.The experiment was carried out under a confocal microscope equipped with an integrated incubator at 37 °C to allow fluorescence intensity quantification at different digestion time points (roughly every 12 s). There was an increase of the fluorescence intensity for the different concentrations studied (Figure 20A-E). At the 2 and 5 μg·mL^{-1} concentrations, the increase of the fluorescence intensity was almost negligible and seemed to become more prominent from 10 μg·mL^{-1} to 50 μg·mL^{-1} which are in agreement with the results from Haan *et al.*[135]. Interestingly, for the higher concentration studied (100 μg·mL^{-1}) a quenching of the fluorescence intensity was observed in the digestion-chip (Figure S2). Figure 20F shows that digestion rates increased with substrate concentration leading to a near-saturation at 50 μg·mL^{-1} where all enzymes are completely bonded to the substrate to form an enzyme–substrate complex. This evidenced the enzyme-catalysis reaction and a typical Michaelis-Menten behaviour in the miniaturised digestive system. Control experiment without enzymes in both gastric and intestinal digestion did not lead to a fluorescence increase (data not shown).

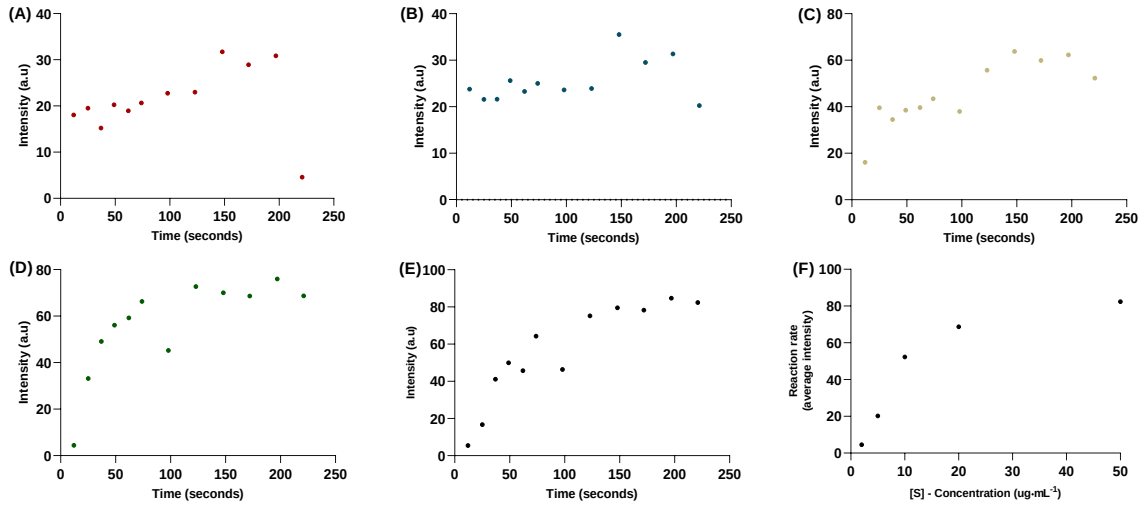

Figure 20. Enzymatic kinetics studies were performed throughout the microfluidic channel to demonstrate the catalysis function. The solution containing the varying concentration of substrate, [S], was introduced in one micromixer inlet, and the simulant gastric fluid containing a fixed concentration of enzyme, [E], was introduced in the other inlet. Fluorescence signals of casein-catalysis digestion of (A) 2 μg·mL^{-1}, (B) 5 μg·mL^{-1}, (C) 10 μg·mL^{-1}, (D) 20 μg·mL^{-1} and (E) 50 μg·mL^{-1} of substrate in the stomach compartment and (F) fluorescence intensity as a function of substrate concentration in the end of the digestion-chip. Values show the measurement of one independent experiment.

4.3.3 On-chip digestion vs static *in vitro* protocol

The same casein reported was digested following the standardised INFOGEST static digestion protocol[129,136] in order to compare the digestion performed on the digestion-chip with a well-established static *in vitro* digestion model. Figure 21 shows fluorescence intensity values every 30 min of digestion collected from the reaction vessel. At 1 $\mu g.mL^{-1}$ of casein concentration, the digestion reached a plateau after 90 min during the gastric phase which means that the substrate was completely converted into product; however, the addition of SIF (100 $U \cdot mL^{-1}$ pancreatin) leads to an increase of the fluorescence intensity reaching another plateau within 30 min of digestion. This outcome indicates that the pepsin-digest residue could be further hydrolysed by pancreatin.[137] At a substrate concentration of 10 $\mu g.mL^{-1}$, digestion plateau was not found during the gastric phase although the fluorescence intensity seemed to gradually decrease with time. Moreover, the addition of SIF lead again to a major increase of fluorescence intensity showing afterwards a plateau at 210 min of digestion. Here, the differences between the fluorescence intensity values (~5,000 *vs* ~50,000) between the two concentrations (1 and 10 $\mu g \cdot mL^{-1}$) over 240 min demonstrate a direct correlation between the fluorescence and amount of casein digested. Interestingly, the digestion in the digestion-chip had an average fluorescence intensity of 17,917 ± 3,871 (Mean ± SD, N=7; Figure 21). The extension of digestion was considerably lower than what was observed in the INFOGEST method (48016.2 ± 9421.5 corresponding to the mean ± SD, N=10); however, a good reproducibility was observed in the digestion-chip. This outcome raises the fact of the reaction stopped before the substrate had been converted into smaller peptides. To understand what happened, SGF and SIF with freshly prepared pepsin and pancreatin, respectively, were added to the output of the digestion-chip and allowed to react at 37 °C off-chip (24-well plate) for 60 min. An increase of the fluorescence intensity was not observed suggesting that the lower extension of digestion in the digestion-chip was not due to enzyme inactivation. It was also hypothesised a change of pH while the solutions were flowing through the miniaturised system. Thus, the pH of the output solutions from the gastric and intestinal phase were measured and displayed values of 3.19 and 7.23 which were not significantly different from the initial digestion solutions. Finally, when casein digested off-chip was flowed through the digestion-chip was observed the presence of casein aggregates (Figure S3) which explain the decrease of 13% in the relative fluorescence intensity. This outcome contributes to the lower extension of digestion but do not explain the difference of 50% when compared to the *in vitro* standard INFOGEST method.

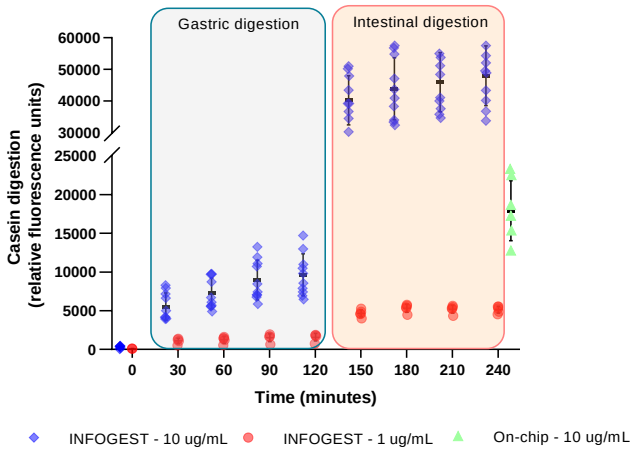

Figure 21. Extension of digestion following the static INFOGEST protocol of casein reporter molecule at 1 and 10 µg·mL^{-1} and its comparison with the end-point of a full digestion of using our digestion-chip (green triangles).

4.3.4 Time-resolved digestion on-chip

10 µg.mL^{-1} of casein and simulant fluids were flowed through the digestion-chip at different flow rates ranging from 12 up to 1152 µL·h^{-1} to obtain a time-resolved digestion leading to decreased incubation times. For the time-resolved intestinal digestion, the gastric phase was first digested off-chip and then introduced into the digestion-chip, as chyme.

Figure 22 shows that the digestion kinetics profile within the first 60 min was similar to those found in the static INFOGEST method. From 60 min onwards, the fluorescence intensity reached a plateau or even underwent a slight decrease which could be associated to a deterioration of the hydrolysed (fluorescent) casein. In the intestinal phase a significant increase in the fluorescence intensity was observed and slightly increased over time. The degradation effect of the substrate seems to be less prominent during the intestinal phase owing to the higher fluorescence intensity values, where a minimal decrease is considered almost negligible.

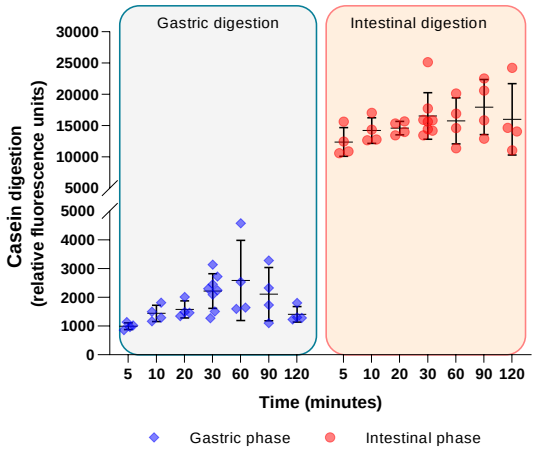

Figure 22. Time-resolved digestion obtained on-chip by varying the flow rates (12-1152 μL·h^{-1}) of the sample and simulated digestion fluids thus attaining different incubation times.

The results shown herein represent full digestions (oral, gastric and intestinal phases) using the digestion-chip and time-resolved digestions at either the gastric or intestinal phases yielding a significant potential for bioaccessibility studies of valuable samples. Nevertheless, the use of alternative materials for device fabrication, such as polymethyl methacrylate should be envisaged to obtain improved on-chip digestion avoid some of the drawbacks referred herein.

4.4 Cell Seeding on-chip

The gut-chip was designed to recapitulate the 3D architecture of the human intestine in order to provide a more physiologically relevant model. Caco-2 cells were grown either on Transwell inserts or in the gut-chip under continuous flow. The morphology of the cell monolayer in both systems was evaluated by immunocytochemistry using an antibody against the tight junction protein (occludin), a rhodamine-labelled phalloidin and DAPI to stain F-actin and nucleus, respectively.

Figure 23 shows the differentiation of Caco-2 cells on Transwell inserts at 7, 14 and 21 days of culture. Here, a confluent epithelial monolayer with well-developed tight junctions was confirmed after 21 days of culture, as reported in the literature[138].

For on-chip cell culture, firstly a functional coating of the porous PDMS membrane had to be performed given that cells do not adhere to unmodified PDMS. The adherence and metabolic activity of Caco-2 was tested on PDMS-coated 24-well plates. Caco-2 cells did not adhere and were significantly less metabolically active when cultured on unmodified PDMS when compared to the tissue culture polystyrene (TCPS), used as positive control (Figure 24). In contrast, when the PDMS surface was oxidised by oxygen plasma treatment, cell adhesion was improved. However, oxygen plasma modification is transient. The best results were observed when PDMS was coated with an extracellular matrix (ECM) mixture of 30

μg·mL^{-1} collagen type-I and 100 μg·mL^{-1} Matrigel (Figure S4). However, when cultured on-chip following a coating with the same ECM mixture, cells failed to adhere. Here, it was hypothesised that the ECM coating was washed away with flow from the surface of the PDMS membrane. To address this issue, a pre-treatment with a bi-functional crosslinker (sulfo-SANPAH) previously reported in the literature[139] was tested aiming to chemically bond the ECM coating on the membrane. Figure 25 shows immunocytochemistry of laminin (the main component of matrigel) and demonstrates that the pre-treatment with sulfo-SANPAH efficiently retained the ECM mixture on the device. Under these conditions, Caco-2 cells were able to adhere and proliferate on the ECM-coated PDMS membrane, as shown in Figure 26. The continuous flow appeared to influence cellular polarisation with basal nucleus (columnar shape) resulting in a thicker monolayer as can be seen in the orthogonal views (Figure 26). Therefore, application of flow in the apical cell surface enhances cell differentiation which was noticed by the increase in height and polarisation of these cells under fluid flow, while cells in the Transwell systems remained flat even after 3 weeks, as can be confirmed by the orthogonal images in Figure 27.

The integration of cyclic strain with fluid flow would enhance cellular differentiation resembling the morphology and function of normal intestinal villi[95]. Kim and colleagues also showed that Caco-2 cells in the microsystem with or without mechanical strain displayed higher TEER values compared to the cells grown under static conditions. Moreover, the apparent permeability coefficient (P_{app}) of the intestinal epithelium was measured and they found that the additional application of cyclic mechanical strain to the microsystem increased the paracellular permeability[95].

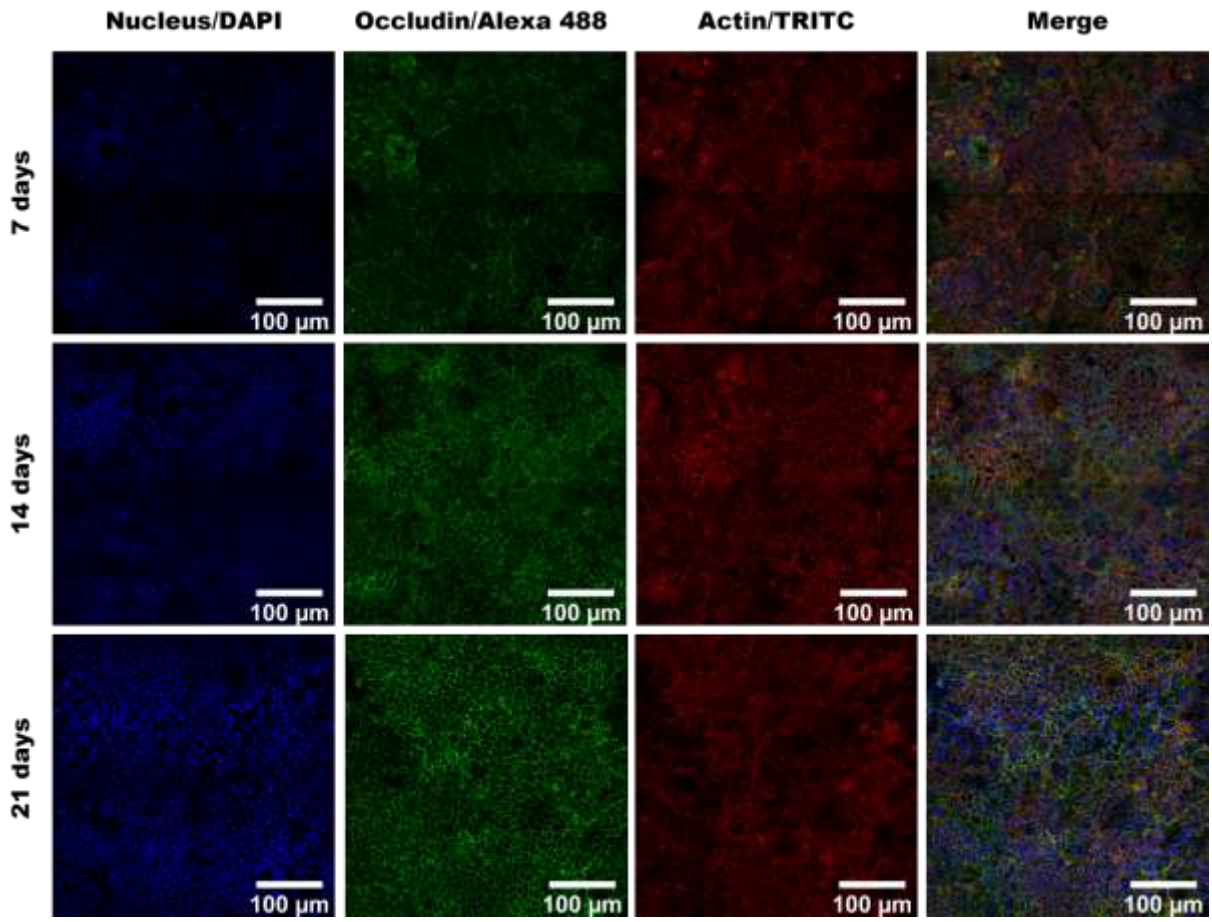

Figure 23. Tile scan confocal micrographs 40x magnification of Caco-2 cells growth on 1 µm pore size transwell® inserts, stained for nuclei (DAPI, blue), tight junctions (occludin, green) and actin filaments (phalloidin, red). Images were acquired after 7, 14 or 21 days in culture.

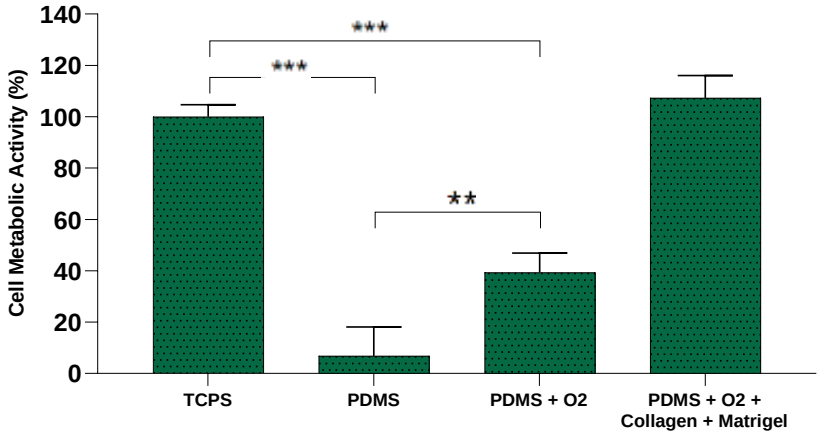

Figure 24. Metabolic activity of Caco-2 cells grown on tissue culture polystyrene (TCPS), unmodified PDMS (PDMS), PDMS treated with oxygen plasma (PDMS + O_2) and PDMS treated with oxygen plasma and coated with ECM (30 µg·mL^{-1} collagen type-I and 100 µg·mL^{-1} Matrigel) (PDMS + O_2 + Collagen + Matrigel) after 48 h. The cell metabolic activity was determined by the resazurin reduction assay measuring the fluorescence of resorufin (λ_{ex}= 560 nm, λ_{em}= 590 nm). Values show mean and standard deviation of three independent experiments; **p < 0.01;***p < 0.001 with p-values obtained using the Student's t-test that followed a normal distribution according to the Shapiro-Wilk test.

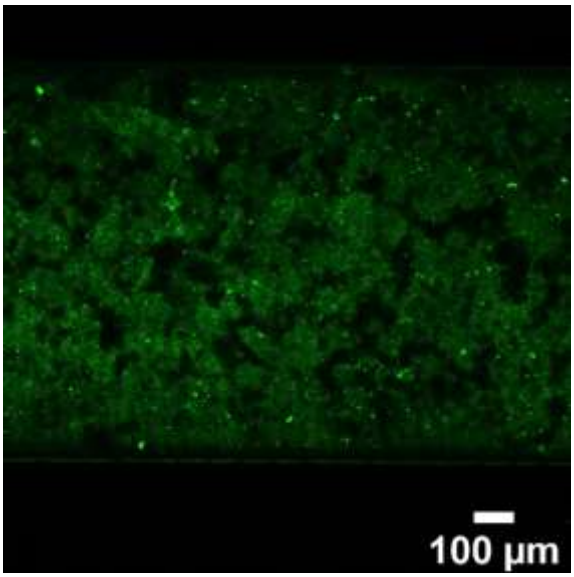

Figure 25. Confocal image of ECM coating on PDMS membrane stained against laminin (the main component of matrigel) in the gut-chip.

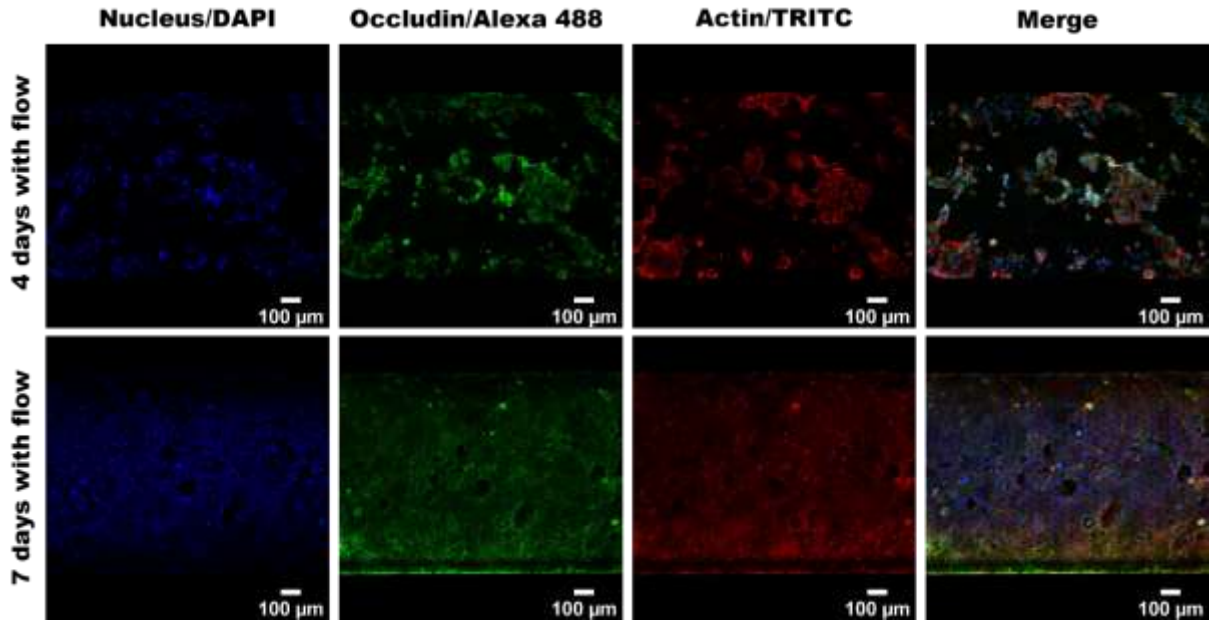

Figure 26. Confocal micrographs 10x magnification of Caco-2 cells grown on the gut-chip and stained for nuclei (DAPI, blue), tight junctions (occludin, green) and actin filaments (phalloidin, red). Images were acquired after 4 or 7 days with continuous flow (30 µL·h^{-1}.) in the gut-chip.

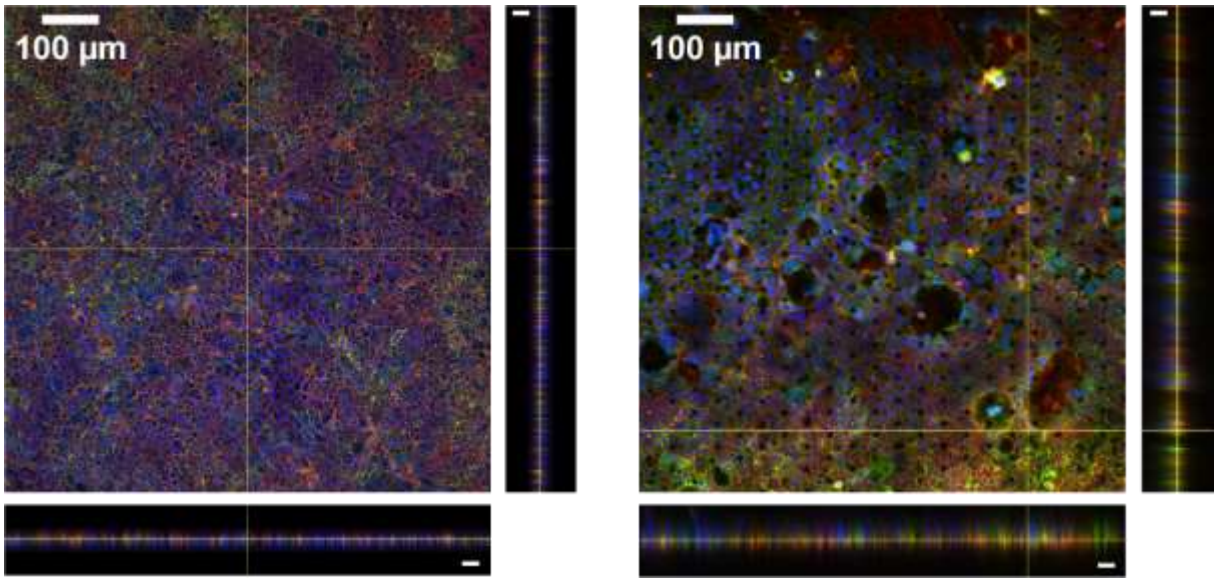

Figure 27. Confocal images and orthogonal cross-section views of Caco-2 cells grown on (A) Transwell inserts after 21 days in culture and (B) gut-chip after 7 days of continuous flow (30 µL·h^{-1}), stained for occludin (green), nuclei (DAPI, blue) and f-actin (red). Bar in the orthogonal images corresponds to 30 µm.

5. Conclusions and Future Perspectives

When using PDMS to fabricate microfluidic-based tools where analytes are quantified, it becomes important to assess the absorption of small molecules by the porous elastomer. The factors affecting the absorption of molecules of interest by PDMS were determined to depend on the nature of the molecule, the solvent, concentrations used, and the residence time determined by the flow rate selected.

A variety of surface and bulk modifications aiming to reduce the absorption of small molecules by PDMS showed a sharp decrease in the polymer hydrophobicity, determined by a reduction of the water contact angle. However, this effect was not stable over the course of 21 days with the elastomer gradually restoring its intrinsic hydrophobicity. Critically, none of the modifications resulted in a significant reduction of the absorption of the studied molecule. This indicated that where molecule absorption is deemed to be problematic, alternative materials should be considered for device fabrication.

On-chip *in vitro* digestion studies showed the capacity to obtain time-resolved digestion kinetics in a fully 'sample-in-answer-out' fashion. Although digestion occurred to a lower extension the digestion-chip when compared to standardised protocols, the on-chip results showed consistency and reproducibility. This could indicate a significant potential to study the bioaccessibility of valuable samples in reduced volumes using automated tools. In future work, the digestion-chip should allow the regulation of the pH and temperature in a controlled manner using an integrated feedback loop.

The cell-based gut-chip integrating continuous flow promoted cell proliferation and the formation of a cellular monolayer on the ECM-coated semi-porous PDMS membrane. In future work, the incorporation of cyclic mechanical strain to mimic peristaltic movements in the device could enhance cell differentiation, including the formation of 3D villi-like structures and increased barrier function. Furthermore, a well-developed intestinal epithelium within the gut-chip can provide conditions for co-culture with microbial flora. These multiple physical and functional features will promote a closer recapitulation of the *in vivo* scenario.

Overall, this study contributed to the establishment of robust *in vitro* tools based on microfluidics to study the digestion and absorption of functional compounds designed for oral administration. A complete human gastrointestinal tract-on-a-chip will help bridge the gap between existing *in vitro* and *in vivo* models with significant potential to be used widely in safety and efficacy studies of bioactive ingredients, in the encapsulated or free form.

6. References

1. Ketnawa, S., Suwannachot, J. & Ogawa, Y. In vitro gastrointestinal digestion of crisphead lettuce: Changes in bioactive compounds and antioxidant potential. *Food Chem.* **311**, 125885 (2020).

2. Lucas-gonzález, R., Viuda-martos, M., Angel, J. & Juana, F. In vitro digestion models suitable for foods: Opportunities for new fields of application and challenges. *Food Res. Int.* **107**, 423–436 (2018).

3. Chai, J. *et al.* The intelligent delivery systems for bioactive compounds in foods: Physicochemical and physiological conditions, absorption mechanisms, obstacles and responsive strategies. *Trends Food Sci. Technol.* **78**, 144–154 (2018).

4. Giaconia, M. A. *et al.* Overcoming restrictions of bioactive compounds biological effects in food using nanometer-sized structures. *Food Hydrocoll.* **107**, 105939 (2020).

5. Bao, C. *et al.* The delivery of sensitive food bioactive ingredients: Absorption mechanisms, influencing factors, encapsulation techniques and evaluation models. *Food Res. Int.* **120**, 130–140 (2019).

6. Cerqueira, M. Â. P. R. *et al.* Nanostructured biobased systems for nutrient and bioactive compounds delivery. in *Nutrient Delivery* 43–85 (Elsevier Inc., 2017).

7. Akbari-Alavijeh, S., Shaddel, R. & Jafari, S. M. Encapsulation of food bioactives and nutraceuticals by various chitosan-based nanocarriers. *Food Hydrocoll.* **105**, 105774 (2020).

8. Ingle, A. P., Shende, S., Gupta, I. & Rai, M. Recent trends in the development of nano-bioactive compounds and delivery systems. in *Biotechnological Production of Bioactive Compounds* 409–431 (Elsevier B.V., 2019).

9. Liu, W., Ye, A., Han, F. & Han, J. Advances and challenges in liposome digestion: Surface interaction, biological fate, and GIT modeling. *Adv. Colloid Interface Sci.* **263**, 52–67 (2019).

10. Brodkorb, A. *et al.* INFOGEST static in vitro simulation of gastrointestinal food digestion. *Nat. Protoc.* **14**, 991–1014 (2019).

11. Minekus, M., Marteau, P., Havenaar, R. & Huis, J. H. J. A multicompartmental dynamic computer-controlled model simulating the stomach and small intestine. *ATLA. Altern. to Lab. Anim.* **23**, 197–209 (1995).

12. Molly, K., Vande Woestyne, M. & Verstraete, W. Development of a 5-step multi-chamber reactor as a simulation of the human intestinal microbial ecosystem. *Appl. Microbiol. Biotechnol.* **39**, 254–258 (1993).

13. Xavier, M. *et al.* Safety and fate of nanomaterials in food: The role of in vitro tests. *Trends Food Sci. Technol.* **109**, 593–607 (2021).

14. Gil-sánchez, I. *et al.* Application of the Dynamic Gastrointestinal Simulator (simgi ®) to assess the impact of probiotic supplementation in the metabolism of grape polyphenols. *Food Res. Int.* **129**, 108790 (2019).

15. Barroso, E., Cueva, C., Peláez, C., Martínez-cuesta, M. C. & Requena, T. Development of human colonic microbiota in the computer-controlled dynamic SIMulator of the GastroIntestinal tract SIMGI. *LWT - Food Sci. Technol.* **61**, 283–289 (2015).

16. Cueva, C. *et al.* Gastrointestinal digestion of food-use silver nanoparticles in the dynamic SIMulator of the GastroIntestinal tract (simgi ®). Impact on human gut microbiota. *Food Chem. Toxicol.* **132**, 110657 (2019).

17. Mahler, G. J., Esch, M. B., Glahn, R. P. & Shuler, M. L. Characterization of a gastrointestinal tract microscale cell culture analog used to predict drug toxicity. *Biotechnol. Bioeng.* **104**, 193–205 (2009).

18. Hidalgo, I. J., Raub, T. J. & Borchardt, R. T. Characterization of the Human Colon Carcinoma Cell Line (Caco-2) as a Model System for Intestinal Epithelial Permeability. *Gastroenterology* **96**, 736–749 (1989).

19. Artursson, P. & Karlsson, J. Correlation between oral drug absorption in humans and apparent drug permeability coefficients in human intestinal epithelial (Caco-2) cells. *Biochem. Biophys. Res. Commun.* **175**, 880–885 (1991).

20. Artursson, P., Palm, K. & Luthman, K. Caco-2 monolayers in experimental and theoretical predictions of drug transport. *Adv. Drug Deliv. Rev.* **46**, 27–43 (2001).

21. Sarmento, B. *et al.* Cell-based in vitro models for predicting drug permeability. *Expert Opin. Drug Metab. Toxicol.* **8**, 607–621 (2012).

22. Antunes, F., Andrade, F., Ferreira, D., Mørck Nielsen, H. & Sarmento, B. Models to Predict Intestinal Absorption of Therapeutic Peptides and Proteins. *Curr. Drug Metab.* **14**, 4–20 (2012).

23. Sun, H., Chow, E. C. Y., Liu, S., Du, Y. & Pang, K. S. The Caco-2 cell monolayer: usefulness and limitations. *Expert Opin. Drug Metab. Toxicol.* **4**, 395–412 (2008).

24. Walter, E. & Kissel, T. Heterogeneity in the human intestinal cell line Caco-2 leads to differences in transepithelial transport. *Eur. J. Pharm. Sci.* **3**, 215–230 (1995).

25. Behrens, I., Stenberg, P., Artursson, P. & Kissel, T. Transport of lipophilic drug molecules in a new mucus-secreting cell culture model based on HT29-MTX cells. *Pharm. Res.* **18**, 1138–1145 (2001).

26. Lozoya-Agullo, I. *et al.* Usefulness of Caco-2/HT29-MTX and Caco-2/HT29-MTX/Raji B Coculture Models To Predict Intestinal and Colonic Permeability Compared to Caco-2 Monoculture. *Mol. Pharm.* **14**, 1264–1270 (2017).

27. Hilgendorf, C. *et al.* Caco-2 versus Caco-2/HT29-MTX Co-cultured Cell Lines: Permeabilities Via Diffusion, Inside- and Outside-Directed Carrier-Mediated Transport. *J. Pharm. Sci.* **89**, 63–75 (2000).

28. Béduneau, A. *et al.* A tunable Caco-2/HT29-MTX co-culture model mimicking variable permeabilities of the human intestine obtained by an original seeding procedure. *Eur. J. Pharm. Biopharm.* **87**, 290–298 (2014).

29. Mahler, G. J., Shuler, M. L. & Glahn, R. P. Characterization of Caco-2 and HT29-MTX cocultures in an in vitro digestion/cell culture model used to predict iron bioavailability. *J. Nutr. Biochem.* **20**, 494–502 (2009).

30. Walter, E., Janich, S., Roessler, B. J., Hilfinger, J. M. & Amidon, G. L. HT29-MTX/Caco-2 Cocultures as an in Vitro Model for the Intestinal Epithelium: In Vitro–in Vivo Correlation with Permeability Data from Rats and Humans. *J. Pharm. Sci.* **85**, 1070–1076 (1996).

31. Araújo, F. *et al. In vitro* M-like cells genesis through a tissue-engineered triple-culture intestinal model. *J. Biomed. Mater. Res. Part B Appl. Biomater.* **104**, 782–788 (2016).

32. Pereira, C., Araújo, F., Barrias, C. C., Granja, P. L. & Sarmento, B. Dissecting stromal-epithelial interactions in a 3D in vitro cellularized intestinal model for permeability studies. *Biomaterials* **56**, 36–45 (2015).

33. Alam, K. *et al.* Recent advances in microfluidic technology for manipulation and analysis of biological cells (2007–2017). *Anal. Chim. Acta* **1044**, 29–65 (2018).

34. Björnmalm, M., Yan, Y. & Caruso, F. Engineering and evaluating drug delivery particles in microfluidic devices. *J. Control. Release* **190**, 139–149 (2014).

35. Jo, M. C. & Guldiken, R. Effects of polydimethylsiloxane (PDMS) microchannels on surface acoustic wave-based microfluidic devices. *Microelectron. Eng.* **113**, 98–104 (2014).

36. Hassan, S. & Zhang, Y. S. Microfluidic technologies for local drug delivery. in *Microfluidics for Pharmaceutical Applications* 281–305 (Elsevier Inc., 2019).

37. Kimura, N., Maeki, M. & Tokeshi, M. Microfabrication and microfluidic devices for drug delivery. in *Microfluidics for Pharmaceutical Applications* 123–136 (Elsevier Inc., 2019).

38. Jammes, F. C. & Maerkl, S. J. How single-cell immunology is benefiting from microfluidic technologies. *Microsystems Nanoeng.* **6**, 45 (2020).

39. Baldacchini, T. Three-Dimensional Microfabrication by Two-Photon Polymerization. in *Generating Micro- and Nanopatterns on Polymeric Materials* 107–140 (Elsevier Inc., 2011).

40. Torino, S., Corrado, B., Iodice, M. & Coppola, G. Pdms-based microfluidic devices for cell culture. *Inventions* **3**, 1–14 (2018).

41. Squires, T. M. & Quake, S. R. Microfluidics: Fluid physics at the nanoliter scale. *Acta Phys. Pol. A* **77**, 977–1026 (2005).

42. Convery, N. & Gadegaard, N. 30 years of microfluidics. *Micro Nano Eng.* **2**, 76–91 (2019).

43. Lei, K. F. Materials and Fabrication Techniques for Nano- and Microfluidic devices. in *RSC Detection Science* 1–28 (2015).

44. Panyam, J., Zhou, W., Prabha, S., Sahoo, S. K. & Labhasetwar, V. Rapid endo-lysosomal escape of poly(dl-lactide-co-glycolide) nanoparticles: implications for drug and gene delivery. *FASEB J.* **16**, 1217–1226 (2002).

45. Nge, P. N., Rogers, C. I. & Woolley, A. T. Advances in Microfluidic Materials, Functions, Integration, and Applications. *Chem. Rev.* **113**, 2550–2583 (2013).

46. Hou, X. *et al.* Interplay between materials and microfluidics. *Nat. Rev. Mater.* **2**, 17016 (2017).

47. McCreedy, T. Fabrication techniques and materials commonly used for the production of microreactors and micro total analytical systems. *TrAC - Trends Anal. Chem.* **19**, 396–401 (2000).

48. Wlodarczyk, K. L., Hand, D. P. & Maroto-Valer, M. M. Maskless, rapid manufacturing of glass microfluidic devices using a picosecond pulsed laser. *Sci. Rep.* **9**, 1–13 (2019).

49. Weng, X., Kang, Y., Guo, Q., Peng, B. & Jiang, H. Recent Advances in Thread-based Microfluidics

for Diagnostic Applications. *Biosens. Bioelectron.* **132**, 171–185 (2019).

50. Lim, W. Y., Goh, B. T. & Khor, S. M. Microfluidic paper-based analytical devices for potential use in quantitative and direct detection of disease biomarkers in clinical analysis. *J. Chromatogr. B* **1060**, 424–442 (2017).

51. Juang, Y., Chen, P. & Wang, Y. Rapid fabrication of microfluidic paper-based analytical devices by microembossing. *Sensors Actuators B. Chem.* **283**, 87–92 (2018).

52. Martinez, A. W., Phillips, S. T., Whitesides, G. M. & Carrilho, E. Diagnostics for the developing world: Microfluidic paper-based analytical devices. *Anal. Chem.* **82**, 3–10 (2010).

53. Trotta, G., Volpe, A., Ancona, A. & Fassi, I. Flexible micro manufacturing platform for the fabrication of PMMA microfluidic devices. *J. Manuf. Process.* **35**, 107–117 (2018).

54. Wan, A. M. D., Devadas, D. & Young, E. W. K. Recycled Polymethylmethacrylate (PMMA) Microfluidic Devices. *Sensors Actuators B. Chem.* **253**, 738–744 (2017).

55. Mono, R. & Angnes, L. Utilisation of micro- and nanoscaled materials in microfluidic analytical devices. *Microchem. J.* **119**, 159–168 (2015).

56. Whitesides, G. M. The origins and the future of microfluidics. *Nature* **442**, 368–373 (2006).

57. Stankova, N. E. *et al.* Optical properties of polydimethylsiloxane (PDMS) during nanosecond laser processing. *Appl. Surf. Sci.* **374**, 96–103 (2016).

58. Gökaltun, A., Kang, Y. B. (Abraham), Yarmush, M. L., Usta, O. B. & Asatekin, A. Simple Surface Modification of Poly(dimethylsiloxane) via Surface Segregating Smart Polymers for Biomicrofluidics. *Sci. Rep.* **9**, 1–14 (2019).

59. Torun, I., Ruzi, M., Er, F. & Onses, M. S. Superhydrophobic coatings made from biocompatible polydimethylsiloxane and natural wax. *Prog. Org. Coatings* **136**, 105279 (2019).

60. Bélanger, M. C. & Marois, Y. Hemocompatibility, biocompatibility, inflammatory and in vivo studies of primary reference materials low-density polyethylene and polydimethylsiloxane: A review. *J. Biomed. Mater. Res.* **58**, 467–477 (2001).

61. Ionescu, M. *et al.* Enhanced biocompatibility of PDMS (polydimethylsiloxane) polymer films by ion irradiation. *Nucl. Instruments Methods Phys. Res. Sect. B Beam Interact. with Mater. Atoms* **273**, 161–163 (2012).

62. Halldorsson, S., Lucumi, E., Gómez-sjöberg, R. & Fleming, R. M. T. Advantages and challenges of micro fl uidic cell culture in polydimethylsiloxane devices. *Biosens. Bioelectron.* **63**, 218–231 (2015).

63. Berthier, E., Young, E. W. K. & Beebe, D. Engineers are from PDMS-land, biologists are from polystyrenia. *Lab Chip* **12**, 1224–1237 (2012).

64. Gale, B. K. *et al.* Low-Cost MEMS Technologies. in *Reference Module in Materials Science and Materials Engineering* 1–32 (Elsevier Inc, 2016).

65. Wolf, M. P., Salieb-Beugelaar, G. B. & Hunziker, P. PDMS with designer functionalities—Properties, modifications strategies, and applications. *Prog. Polym. Sci.* **83**, 97–134 (2018).

66. Oyama, T. G., Oyama, K. & Taguchi, M. A simple method for production of hydrophilic, rigid, and

sterilized multi-layer 3D integrated polydimethylsiloxane microfluidic chips. *Lab Chip* **20**, 2354–2363 (2020).

67. Moraes, C., Chen, J. H., Sun, Y. & Simmons, C. A. Microfabricated arrays for high-throughput screening of cellular response to cyclic substrate deformation. *Lab Chip* **10**, 227–234 (2010).

68. Tan, J. L. *et al.* Cells lying on a bed of microneedles: An approach to isolate mechanical force. *Proc. Natl. Acad. Sci. U. S. A.* **100**, 1484–1489 (2003).

69. Murrell, M., Kamm, R. & Matsudaira, P. Substrate viscosity enhances correlation in epithelial sheet movement. *Biophys. J.* **101**, 297–306 (2011).

70. Grover, W. H., Ivester, R. H. C., Jensen, E. C. & Mathies, R. A. Development and multiplexed control of latching pneumatic valves using microfluidic logical structures. *Lab Chip* **6**, 623–631 (2006).

71. Song, J. W. *et al.* Computer-controlled microcirculatory support system for endothelial cell culture and shearing. *Anal. Chem.* **77**, 3993–3999 (2005).

72. Jensen, E. C., Zeng, Y., Kim, J. & Mathies, R. A. Microvalve enabled digital microfluidic systems for high-performance biochemical and genetic analysis. *JALA - J. Assoc. Lab. Autom.* **15**, 455–463 (2010).

73. Kang, C., Roh, C. & Overfelt, R. A. Pressure-driven deformation with soft polydimethylsiloxane (PDMS) by a regular syringe pump: Challenge to the classical fluid dynamics by comparison of experimental and theoretical results. *RSC Adv.* **4**, 3102–3112 (2014).

74. Lee, J. N., Park, C. & Whitesides, G. M. Solvent Compatibility of Poly(dimethylsiloxane)-Based Microfluidic Devices. *Anal. Chem.* **75**, 6544–6554 (2003).

75. Toepke, M. W. & Beebe, D. J. PDMS absorption of small molecules and consequences in microfluidic applications. *Lab Chip* **6**, 1484–1486 (2006).

76. Adiraj Iyer, M. & Eddington, D. T. Storing and releasing rhodamine as a model hydrophobic compound in polydimethylsiloxane microfluidic devices. *Lab Chip* **19**, 574–579 (2019).

77. Subramani, K. Fabrication of hydrogel micropatterns by soft photolithography. in *Emerging Nanotechnologies for Manufacturing* 279–293 (Elsevier Inc., 2014).

78. Martinez-Duarte, R. & Madou, M. J. SU-8 photolithography and its impact on microfluidics. in *Microfluidics and Nanofluidics Handbook: Fabrication, Implementation, and Applications* 231–268 (2016).

79. Hubenthal, F. Noble Metal Nanoparticles: Synthesis and Optical Properties. in *Comprehensive Nanoscience and Technology* 375–435 (Elsevier, 2011).

80. Quero, J. M., Perdigones, F. & Aracil, C. Microfabrication technologies used for creating smart devices for industrial applications. in *Smart Sensors and MEMS: Intelligent Sensing Devices and Microsystems for Industrial Applications: Second Edition* 291–311 (2018).

81. Li, C.-W. & Wang, G.-J. MEMS manufacturing techniques for tissue scaffolding devices. in *MEMS for Biomedical Applications* 192–217 (2012).

82. Zhang, F., Fu, Y. & Yu, X. Microfluidics and Interfacial Chemistry in the Atmosphere. in *Physical Chemistry of Gas-Liquid Interfaces* 245–270 (Elsevier Inc., 2018).

83. Nur, O. & Willander, M. Conventional nanofabrication methods. in *Low Temperature Chemical Nanofabrication* 49–86 (2020).

84. Wu, H. *et al.* Fabrication of microfluidic systems in poly(dimethylsiloxane). *Electrophoresis* **21**, 27–40 (2000).

85. Duffy, D. C., McDonald, J. C., Schueller, O. J. A. & Whitesides, G. M. Rapid prototyping of microfluidic systems in poly(dimethylsiloxane). *Anal. Chem.* **70**, 4974–4984 (1998).

86. Agostini, M., Greco, G. & Cecchini, M. Polydimethylsiloxane (PDMS) irreversible bonding to untreated plastics and metals for microfluidics applications. *APL Mater.* **7**, 081108 (2019).

87. Eddings, M. A., Johnson, M. A. & Gale, B. K. Determining the optimal PDMS – PDMS bonding technique for microfluidic devices. *J. Micromechanics Microengineering* **18**, 6 (2008).

88. Marze, S., Algaba, H. & Marquis, M. A microfluidic device to study the digestion of trapped lipid droplets. *Food Funct.* **5**, 1481–1488 (2014).

89. de Haan, P. *et al.* Digestion-on-a-chip: a continuous-flow modular microsystem recreating enzymatic digestion in the gastrointestinal tract. *Lab Chip* **19**, 1599–1609 (2019).

90. Stroock, A. D. *et al.* Chaotic mixer for microchannels. *Science (80-.).* **295**, 647–651 (2002).

91. Bures, J. *et al.* Small intestinal bacterial overgrowth syndrome. *World J. Gastroenterol.* **16**, 2978–2990 (2010).

92. Bein, A. *et al.* Microfluidic Organ-on-a-Chip Models of Human Intestine. *Cell. Mol. Gastroenterol. Hepatol.* **5**, 659–668 (2018).

93. Lee, S. H. & Sung, J. H. Gut-on-a-chip microphysiological systems for the recapitulation of the gut microenvironment. in *Organ-on-a-chip: Engineered Microenvironments for Safety and Efficacy Testing* 295–310 (Elsevier Inc., 2019).

94. Kim, H. J., Li, H., Collins, J. J. & Ingber, D. E. Contributions of microbiome and mechanical deformation to intestinal bacterial overgrowth and inflammation in a human gut-on-a-chip. *Proc. Natl. Acad. Sci. U. S. A.* **113**, 7–15 (2016).

95. Kim, H. J., Huh, D., Hamilton, G. & Ingber, D. E. Human gut-on-a-chip inhabited by microbial flora that experiences intestinal peristalsis-like motions and flow. *Lab Chip* **12**, 2165–2174 (2012).

96. Brand, R. M., Hannah, T. L., Mueller, C., Cetin, Y. & Hamel, F. G. Novel system to study the impact of epithelial barriers on cellular metabolism. *Ann. Biomed. Eng.* **28**, 1210–1217 (2000).

97. Brand, R. M., Hannah, T. L., Mueller, C., Cetin, Y. & Hamel, F. G. A Novel System to Study the Impact of Epithelial Barriers on Cellular Metabolism. *Ann. Biomed. Eng.* **28**, 1210–1217 (2000).

98. Kimura, H., Yamamoto, T., Sakai, H., Sakai, Y. & Fujii, T. An integrated microfluidic system for long-term perfusion culture and on-line monitoring of intestinal tissue models. *Lab Chip* **8**, 741–746 (2008).

99. Kimura, H., Ikeda, T., Nakayama, H., Sakai, Y. & Fujii, T. An On-Chip Small Intestine–Liver Model for Pharmacokinetic Studies. *J. Lab. Autom.* **20**, 265–273 (2015).

100. Imura, Y., Asano, Y., Sato, K. & Yoshimura, E. A Microfluidic System to Evaluate Intestinal Absorption. *Anal. Sci.* **25**, 1403–1407 (2009).

101. Imura, Y., Sato, K. & Yoshimura, E. Micro Total Bioassay System for Ingested Substances: Assessment of Intestinal Absorption, Hepatic Metabolism, and Bioactivity. *Anal. Chem.* **82**, 9983–9988 (2010).

102. Imura, Y., Yoshimura, E. & Sato, K. Micro Total Bioassay System for Oral Drugs: Evaluation of Gastrointestinal Degradation, Intestinal Absorption, Hepatic Metabolism, and Bioactivity. *Anal. Sci.* **28**, 197–199 (2012).

103. McAuliffe, G. J., Chang, J. Y., Glahn, R. P. & Shuler, M. L. Development of a gastrointestinal tract microscale cell culture analog to predict drug transport. *Mol. Cell. Biomech.* **5**, 119–132 (2008).

104. Esch, M. B., Mahler, G. J., Stokol, T. & Shuler, M. L. Body-on-a-chip simulation with gastrointestinal tract and liver tissues suggests that ingested nanoparticles have the potential to cause liver injury. *Lab Chip* **14**, 3081–3092 (2014).

105. Esch, M. B., Ueno, H., Applegate, D. R. & Shuler, M. L. Modular, pumpless body-on-a-chip platform for the co-culture of GI tract epithelium and 3D primary liver tissue. *Lab Chip* **16**, 2719–2729 (2016).

106. Chen, H. J., Miller, P. & Shuler, M. L. A pumpless body-on-a-chip model using a primary culture of human intestinal cells and a 3D culture of liver cells. *Lab Chip* **18**, 2036–2046 (2018).

107. Kostadinova, R. *et al.* A long-term three dimensional liver co-culture system for improved prediction of clinically relevant drug-induced hepatotoxicity. *Toxicol. Appl. Pharmacol.* **268**, 1–16 (2013).

108. Ramadan, Q. *et al.* NutriChip: nutrition analysis meets microfluidics. *Lab Chip* **13**, 196–203 (2013).

109. Shah, P. *et al.* A microfluidics-based in vitro model of the gastrointestinal human–microbe interface. *Nat. Commun.* **7**, 11535 (2016).

110. Huh, D. *et al.* Reconstituting organ-level lung functions on a chip. *Science* **328**, 1662–1668 (2010).

111. Jang, K.-J. *et al.* Human kidney proximal tubule-on-a-chip for drug transport and nephrotoxicity assessment. *Integr. Biol.* **5**, 1119–1129 (2013).

112. Torisawa, Y. *et al.* Bone marrow–on–a–chip replicates hematopoietic niche physiology in vitro. *Nat. Methods* **11**, 663–669 (2014).

113. Herland, A. *et al.* Distinct Contributions of Astrocytes and Pericytes to Neuroinflammation Identified in a 3D Human Blood-Brain Barrier on a Chip. *PLoS One* **11**, 0150360 (2016).

114. Kim, H. J. & Ingber, D. E. Gut-on-a-Chip microenvironment induces human intestinal cells to undergo villus differentiation. *Integr. Biol.* **5**, 1130–1140 (2013).

115. Kim, H. J., Lee, J., Choi, J.-H., Bahinski, A. & Ingber, D. E. Co-culture of Living Microbiome with Microengineered Human Intestinal Villi in a Gut-on-a-Chip Microfluidic Device. *J. Vis. Exp.* 54344 (2016).

116. Villenave, R. *et al.* Human Gut-On-A-Chip Supports Polarized Infection of Coxsackie B1 Virus In Vitro. *PLoS One* **12**, 0169412 (2017).

117. Jalili-Firoozinezhad, S. *et al.* Complex human gut microbiome cultured in anaerobic human intestine chips. *Nat. Biomed. Eng.* **7**, 520–531 (2019).

118. Kasendra, M. *et al.* Development of a primary human Small Intestine-on-a-Chip using biopsy-derived organoids. *Sci. Rep.* **8**, 2871 (2018).

119. Maschmeyer, I. *et al.* A four-organ-chip for interconnected long-term co-culture of human intestine, liver, skin and kidney equivalents. *Lab Chip* **15**, 2688–2699 (2015).

120. Hosic, S. *et al.* Rapid prototyping of a multilayer microphysiological system for primary human intestinal epithelial culture. *BioRxiv* (2018).

121. Dawson, A. *et al.* A microfluidic chip based model for the study of full thickness human intestinal tissue using dual flow. *Biomicrofluidics* **10**, 064101 (2016).

122. Trietsch, S. J. *et al.* Membrane-free culture and real-time barrier integrity assessment of perfused intestinal epithelium tubes. *Nat. Commun.* **8**, 262 (2017).

123. Guo, Y. *et al.* A Biomimetic Human Gut-on-a-Chip for Modeling Drug Metabolism in Intestine. *Artif. Organs* **12**, 1196–1205 (2018).

124. Pocock, K. *et al.* Intestine-on-a-Chip Microfluidic Model for Efficient in Vitro Screening of Oral Chemotherapeutic Uptake. *ACS Biomater. Sci. Eng.* **3**, 951–959 (2017).

125. Jalili-Firoozinezhad, S. *et al.* Modeling radiation injury-induced cell death and countermeasure drug responses in a human Gut-on-a-Chip. *Cell Death Dis.* **9**, 223 (2018).

126. Wu, Z. & Hjort, K. Surface modification of PDMS by gradient-induced migration of embedded Pluronic. *Lab Chip* **9**, 1500–1503 (2009).

127. Eddington, D. T., Puccinelli, J. P. & Beebe, D. J. Thermal aging and reduced hydrophobic recovery of polydimethylsiloxane. *Sensors Actuators, B Chem.* **114**, 170–172 (2006).

128. Gomez-Sjoberg, R., Leyrat, A. A., Houseman, B. T., Shokat, K. & Quake, S. R. Biocompatibility and reduced drug absorption of sol-gel-treated poly(dimethyl siloxane) for microfluidic cell culture applications. *Anal. Chem.* **82**, 8954–8960 (2010).

129. Brodkorb, A. *et al.* INFOGEST static in vitro simulation of gastrointestinal food digestion. *Nat. Protoc.* **14**, 991–1014 (2019).

130. Wang, J. D., Douville, N. J., Takayama, S. & Elsayed, M. Quantitative analysis of molecular absorption into PDMS microfluidic channels. *Ann. Biomed. Eng.* **40**, 1862–1873 (2012).

131. Standley D. Fowler and Phillip Greenspan. Application of Nile Red, a Fluorescent Hydrophobic Probe, fot the Detection of Neutral Lipid Deposits in Tissue Sections: Comparison with Oil Red. *J. Histochem. Cytochem.* **33**, 833–836 (1985).

132. Silva, H. D. *et al.* Evaluating the behaviour of curcumin nanoemulsions and multilayer nanoemulsions during dynamic in vitro digestion. *J. Funct. Foods* **48**, 605–613 (2018).

133. Maheshwari, N., Kottantharayil, A., Kumar, M. & Mukherji, S. Long term hydrophilic coating on poly(dimethylsiloxane) substrates for microfluidic applications. *Appl. Surf. Sci.* **257**, 451–457 (2010).

134. Brewer, Bryson, Gao, Yandong and Li, D. A study of small molecule absorption in polydimethylsiloxane. in *ASME 2012 Third International Conference on Micro/Nanoscale Heat and Mass Transfer* 15–19 (2012).

135. de Haan, P. *et al.* Digestion-on-a-chip: a continuous-flow modular microsystem recreating enzymatic digestion in the gastrointestinal tract. *Lab Chip* **19**, 1599–1609 (2019).

136. Minekus, M. *et al.* A standardised static in vitro digestion method suitable for food-an international consensus. *Food Funct.* **5**, 1113–1124 (2014).

137. Akeson, W. R. & Stahmann, M. A. A Pepsin Pancreatin Digest Index of Protein Quality Evaluation. *J. Nutr.* **83**, 257–261 (1964).

138. Le Ferrec, E. *et al.* In vitro models of the intestinal barrier. The report and recommendations of ECVAM Workshop 46. European Centre for the Validation of Alternative methods. *Altern. Lab. Anim.* **29**, 649–68 (2014).

139. Shin, W. *et al.* Robust Formation of an Epithelial Layer of Human Intestinal Organoids in a Polydimethylsiloxane-Based Gut-on-a-Chip Microdevice. *Front. Med. Technol.* **2**, 1–24 (2020).

7. Annexes

Supplementary Information to Materials and Methods: Experimental Design

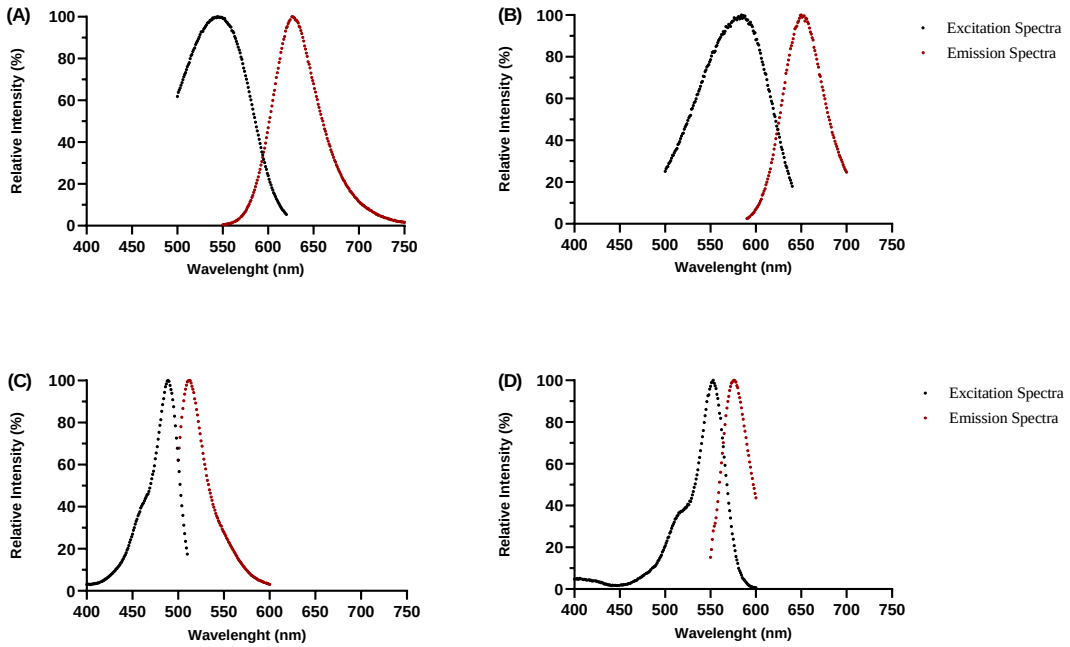

Figure S1. Graphic representation of fluorescence spectra of (A) Nile Red solution in ethanol; (B) Nile Red solution in ethanol/PBS; (D) Fluorescein solution; (D) Rhodamine B solution. The excitation and emission maxima of Nile Red in ethanol (λ_{ex}: 543 nm; λ_{em}: 627 nm), Nile Red in ethanol/PBS (λ_{ex}: 584 nm; λ_{em}: 650 nm); Fluorescein (λ_{ex}: 485 nm; λ_{em}: 515 nm) and Rhodamine B (λ_{ex}: 550 nm; λ_{em}: 580 nm).

Supplementary information to Results and Discussion: On-chip *in vitro* digestion

Table S1. Calculations of the Reynolds number ($Re=\rho \cdot V \cdot D/\mu$) at a *range flow rate* used in the GIT-on-a-chip digestion considering the channel dimensions at the staggered herringbone regions (200 µm x 100 µm), the hydraulic diameter (D) estimated at $2h \cdot w/h+w$. The density (ρ=0.9982x10^3 kg·m^{-3}) and dynamic viscosity (μ=1.002x10^{-3} Pa·s) of water at 20 °C were used.

Flow rate (Q; µL·h^{-1})	Flow velocity (V; m·s^{-1})	Reynolds (Re)
24	3.3x10^{-4}	0.04
48	6.7x10^{-4}	0.09
96	1.3x10^{-3}	0.18
128	1.8x10^{-3}	0.24
192	2.7x10^{-3}	0.35
384	5.3x10^{-3}	0.71
576	8.0x10^{-3}	1.06
1152	1.6x10^{-3}	2.13
2304	3.3x10^{-3}	4.25

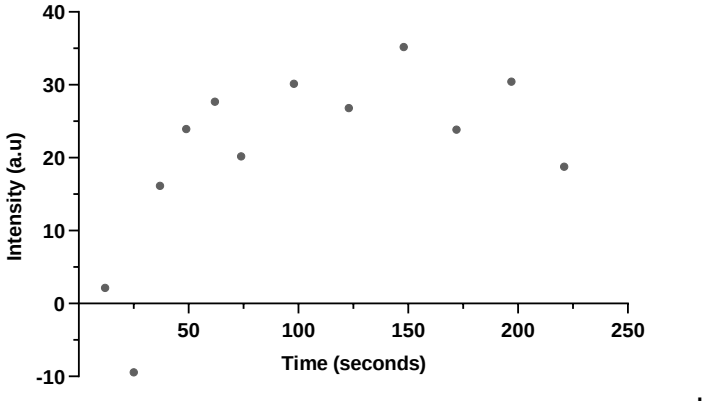

Figure S2. Enzymatic kinetics studies were performed throughout the microfluidic channel to demonstrate the catalysis function. The solution containing the varying concentration of substrate, [S], was introduced in one micromixer inlet, and the gastric simulant fluid containing a fixed concentration of enzyme, [E], was introduced in the other inlet. Fluorescence signals of casein-catalysis digestion of 100 μgmL^{-1} of substrate in the stomach compartment. Values shows the measurements of one independent experiment.

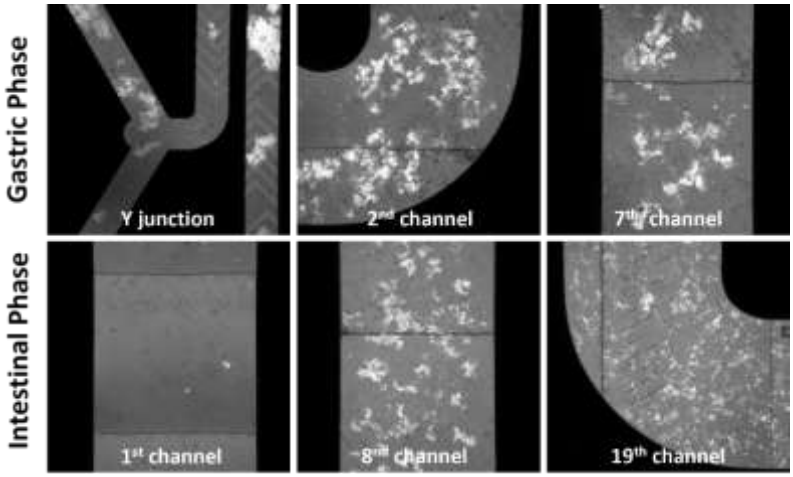

Figure S3. Confocal micrographs showing casein aggregates in the gastric and intestinal chamber after the flow of casein digested off-chip for 300 min.

Supplementary information to Results and Discussion: Cell seeding on-chip

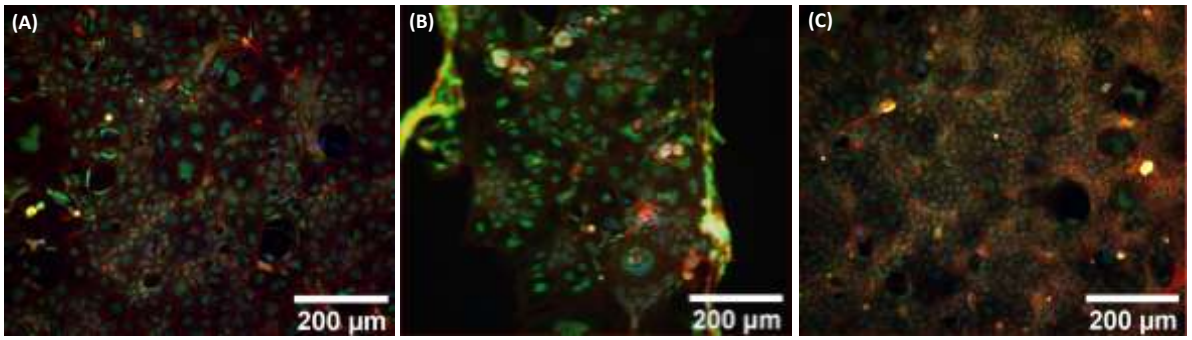

Figure S4. Fluorescence image of Caco-2 cells adherence on (A) tissue culture polystyrene (TCPS), (B) PDMS treated with oxygen plasma (PDMS + O_2) and (C) PDMS treated with oxygen plasma and coated with ECM (30 µg·mL^{-1} collagen type-I and 100 µg·mL^{-1} Matrigel) (PDMS + O_2 + Collagen + Matrigel) after 48 h of culture.